CM² MAGAZINE

第 11 期

南方科技大学海洋磁学中心主编

创刊词

海洋是生命的摇篮，是文明的纽带。地球上最早的生命诞生于海洋，海洋里的生命最终进化成了人类，人类的文化融合又通过海洋得以实现。人因海而兴。

人类对海洋的探索从未停止。从远古时代美丽的神话传说，到麦哲伦的全球航行，再到现代对大洋的科学钻探计划，海洋逐渐从人类敬畏崇拜幻想的精神寄托演变成可以开发利用与科学研究的客观存在。其中，上个世纪与太空探索同步发展的大洋科学钻探计划将人类对海洋的认知推向了崭新的纬度：深海（deep sea）与深时（deep time）。大洋钻探计划让人类知道，奔流不息的大海之下，埋藏的却是亿万年的地球历史。它们记录了地球板块的运动，从而使板块构造学说得到证实；它们记录了地球环境的演变，从而让古海洋学方兴未艾。

在探索海洋的悠久历史中，从大航海时代的导航，到大洋钻探计划中不可或缺的磁性地层学，磁学发挥了不可替代的作用。这不是偶然，因为从微观到宏观，磁性是最基本的物理属性之一，可以说，万物皆有磁性。基于课题组的学科背景和对海洋的理解，我们对海洋的探索以磁学为主要手段，海洋磁学中心因此而生。

海洋磁学中心，简称 CM^2，一为其全名“Centre for Marine Magnetism”的缩写，另者恰与爱因斯坦著名的质能方程 $E = MC^2$ 对称，借以表达我们对科学巨匠的敬仰和对科学的不懈追求。

然而科学从来不是单打独斗的产物。我们以磁学为研究海洋的主攻利器，但绝不仅限于磁学。凡与磁学相关的领域均是我们关注的重点。为了跟踪反映国内外地球科学特别是与磁学有关的地球科学领域的最新研究进展，海洋磁学中心特地主办 CM^2 Magazine，以期与各位地球科学工作者相互交流学习、合作共进！

“海洋孕育了生命，联通了世界，促进了发展”。 21 世纪是海洋科学的时代，由陆向海，让我们携手迈进中国海洋科学的黄金时代！

目 录

1. 石笋记录的中期石器晚期-旧石器晚期西加利利地区的气候和环境变化

翻译人：陈琼 chenq268@mail.sysu.edu.cn

Yasur G, Ayalon A, Matthews A, et al. ***Climatic and environmental conditions in the Western Galilee, during Late Middle and Upper Paleolithic periods, based on speleothems from Manot Cave, Israel****[J].* ***Journal of Human Evolution****, 2019.*

摘要：阿马尔早期技术、黎凡特奥瑞纳技术和黎凡特晚期-奥瑞纳技术等多种石器技术体系并存的现象表明，在旧石器晚期早段以色列加利利西部马诺特洞穴（Manot Cave）内的人类活动活跃。洞穴中与旧石器共生的石笋成为研究该时期的气候变化与加利利西部人类的活动以及迁移模式之间联系的绝佳地质材料。本文报道了四支发育于~75-26.5ka 的石笋记录，其年代范围跨越了末次冰期的大部分时间，并涵盖了该洞穴古人类的活动时期。石笋的碳氧稳定同位素记录（$\delta^{13}C$-$\delta^{18}O$）表明了末次冰期以来该地区的气候环境存在较大波动，记录了 D/O12、D/O10、D/O7 以及 H5 和 H6 等气候事件。这些气候波动使得加利利西部的环境发生显著变化，呈现从茂密的地中海森林到 C4 植被占优势的开阔环境的变化，这与植物孢粉和动物化石记录的环境变化信息一致。在阿马尔早期技术时期，石笋的 $\delta^{13}C$ 呈现显著的正向偏移，而在黎凡特奥瑞纳技术和黎凡特晚期-奥瑞纳技术时期，石笋的 $\delta^{13}C$ 也呈现出正向偏移，表明环境向 C4 植被占优势的开阔草原转化可能对马诺特洞穴地区的石器技术体系（主要为阿马尔早期技术）的发展具有重要作用。

ABSTRACT: Early Ahmarian, Levantine Aurignacian and Post-Levantine Aurignacian archeological assemblages show that the karstic Manot Cave, located 5 km east of the Mediterranean coast in the Western Galilee region of Israel, was intensively occupied during the Early Upper Paleolithic. The coexistence of these rich archaeological layers with speleothems in Manot Cave provides a window of opportunity for determining the relationships between climatic conditions and the nature of human activity and mobility patterns in the Western Galilee region during the Early Upper Paleolithic period. This study, based on four stalagmites that grew almost continuously from ~75 to 26.5 ka, covers most of the last glacial, and overlaps with the human occupation of the cave. The speleothems oxygen ($\delta^{18}O$) and carbon ($\delta^{13}C$) isotopic re-cords indicate that climate and environmental conditions fluctuated during the last glacial, some of which correspond with

Dansgaarde-Oeschger (D-O) cycles 12, 10, 7 and Heinrich (H) events VI and V. Consistent with independent evidence from botanic and faunal remains, these climatic shifts brought about significant environmental changes in the region, ranging from dominant thick Mediterranean forest to more open landscape. A good correlation with less negative $\delta^{13}C$ values is most pronounced during the Early Ahmarian time period, but there was also a change to less negative $\delta^{13}C$ values during the Levantine Aurignacian and Post-Levantine Aurignacian industries in the Levant. These positive $\delta^{13}C$ shifts suggest that environmental transformation towards a more open grassy landscape dominated by C4 vegetation might have played an important role in the development of these cultural entities (mainly the Early Ahmarian) in Manot Cave region.

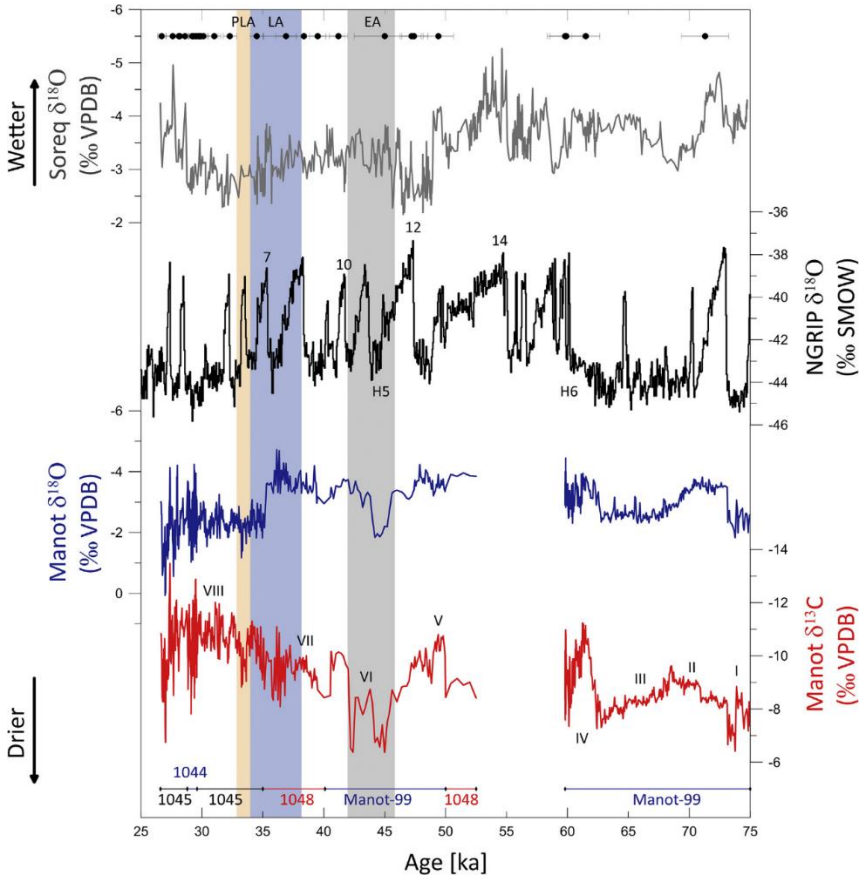

Figure 1. Manot Cave speleothems $\delta^{18}O$ (blue) and $\delta^{13}C$ (red) composite age records plotted with reference to the Soreq Cave (grey; Bar-Matthews et al., 2017) and NGRIP (black) $\delta^{18}O$ records. Periods I-VIII are the growth phases described in the text. The horizontal bars at the base of the diagram mark the portions of the speleothems records used to construct the composite profile. The duration of the Early Ahmarian (EA), Levantine Aurignacian (LA) and Post-Levantine Aurignacian (PLA) cultures (Alex et al., 2017) are indicated by vertical colored bands (grey, light blue, and yellow respectively). Cold Heinrich events H5, H6, and warm-cold Dansgaarde-Oeschger cycles (D/O) 7, 10, 12 and 14 are indicated adjacent to the NGRIP record. The circles with error bars at the top of the diagram indicate the measured U-Th ages of Manot Cave speleothems. Vertical arrows on the left side of the diagram show the wet and dry climatic trends for both isotope systems.

2. 中国南方湖光岩玛珥湖全新世沉积物中年代际至百年尺度的 ^{10}Be 变化

翻译人：张庭伟 zhangtw6@mail2.sysu.edu.cn

Tang L, Zhou W, Wang X, et al. ***Multi-decadal to centennial-scale ^{10}Be variations in Holocene sediments of Huguangyan Maar Lake, South China[J]. Geophysical Research Letters.***

摘要：我们报告了来自中国南方热带-亚热带地区的湖光岩玛珥湖的一根新的全新世钻孔的高分辨率 ^{10}Be 记录，以探测低纬度地区的大气中 ^{10}Be 的产生信号。通过将 ^{10}Be 浓度与钻孔的其他气候指标进行回归分析最小化气候影响之后，我们对残留 ^{10}Be 记录（大气 ^{10}Be 产生率的指标）分别进行 2000 年的低通和高通滤波，成功的分离了地磁场强度和太阳活动的变化。由此产生的 ^{10}Be 记录的地磁场强度总体上可与地磁模型进行比较，而经太阳活动调节后的 ^{10}Be 信号与太阳活动指标具有显著相关性。湖光岩玛珥湖的沉积物中所记录的 ^{10}Be 信号表明，^{10}Be 作为重建太阳活动和地磁场强度变化的指标具有巨大潜力和局限性。

ABSTRACT: We report a new high-resolution Holocene ^{10}Be record from Huguangyan Maar Lake in subtropical-tropical South China, aimed to detect the atmospheric ^{10}Be production signal in low-latitude regions. After minimizing climatic effects by regression analyses between ^{10}Be concentration and climatic proxies from the same archive, we successfully distinguished variations in geomagnetic field intensity and solar activity using 2,000-year low- and high-pass filtering, respectively, of the residual ^{10}Be record (a proxy of the atmospheric ^{10}Be production rate). The resulting ^{10}Be-derived record of geomagnetic field intensity is generally comparable with geomagnetic models, and the solar-modulated ^{10}Be signal shows significant correlations with solar activity proxies. The preservation of ^{10}Be production signal in the sediments of this low-latitude maar lake highlights the largely unexplored potential as well as limitations of ^{10}Be as a tool to reconstruct variations in solar activity and geomagnetic field intensity.

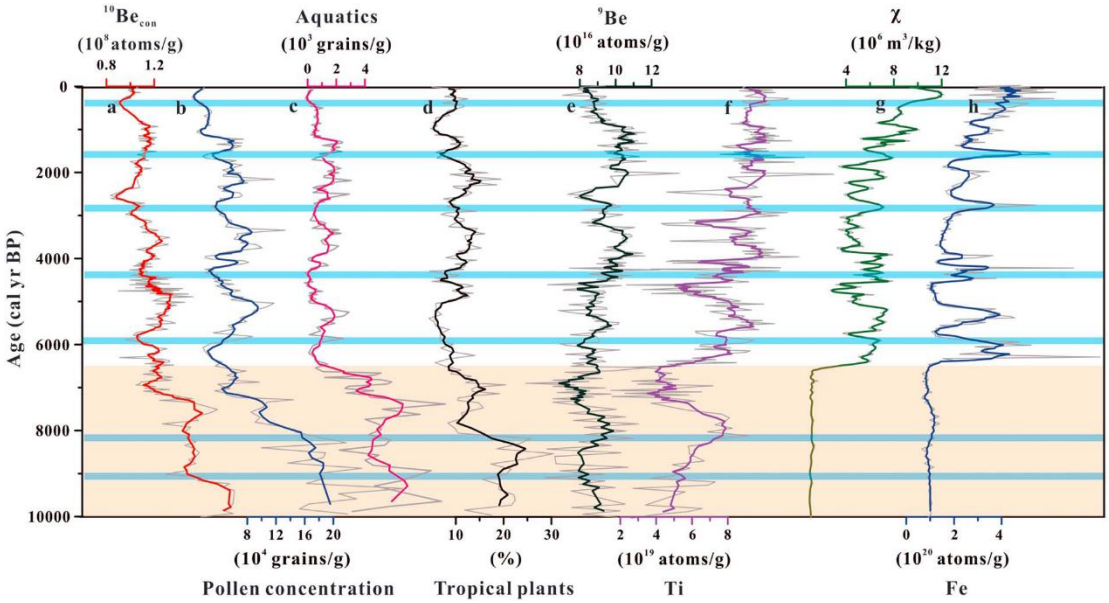

Figure 1. Time series of ^{10}Be concentration ($^{10}Be_{con}$) and paleoenvironmental proxies from Huguangyan Maar Lake since 10 ka. (a) $^{10}Be_{con}$, (b) pollen concentration, (c) pollen sum of aquatic and wetland taxa (Aquatics; Wang et al., 2016), (d) percentage of tropical taxa (Wang et al., 2016), (e) ^9Be concentration, (f) Ti concentration, (g) mass-specific magnetic susceptibility (χ; Wang et al., 2016), and (h) Fe concentration. The gray curves represent the original data, and the colored curves are 5-point moving averages. The horizontal blue bars indicate cooling events associated with Bond cycles (Bond et al., 1997). The interval of the early Holocene climatic optimum is indicated by orange shading.

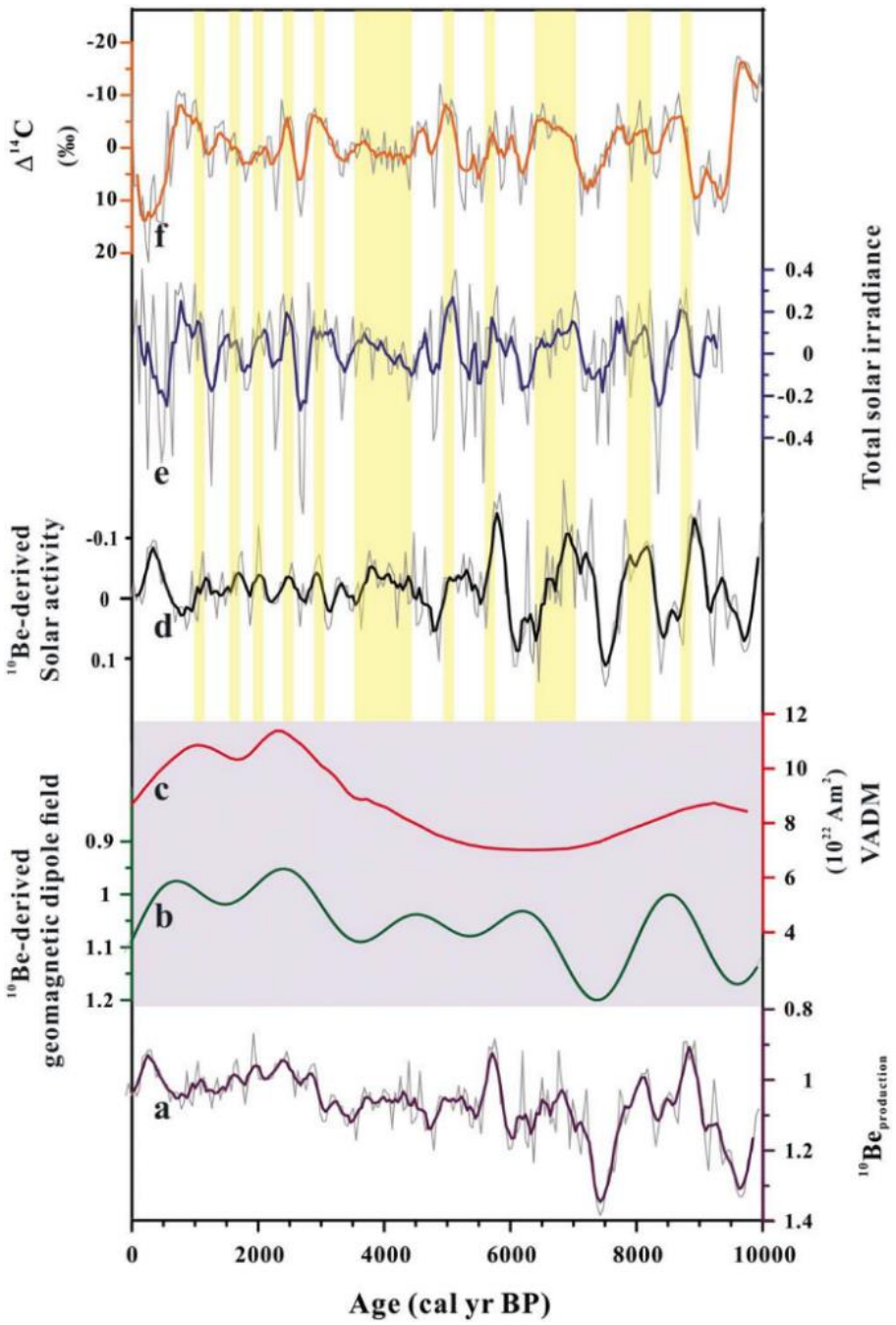

Figure 2. ^{10}Be production rate ($^{10}Be_{con}$ residual), comparisons of ^{10}Be-based geomagnetic intensity and solar activity with geomagnetic dipole field model and recent solar activity reconstructions. Both our ^{10}Be record and proxies of solar activity are 44-year averages. The gray curves represent the original data, and the colored curves are 5-point moving averages. (a) ^{10}Be production signal based on $^{10}Be_{con}$, (b) relative geomagnetic dipole field strength obtained from applying a 2000 yr low-pass filter to the Huguangyan Maar Lake $^{10}Be_{production}$ signal, (c) geomagnetic dipole field strength (Knudsen et al., 2008), (d) record of solar activity from the Huguangyan Maar Lake ^{10}Be record (2000 yr high-pass filter), (e) total solar irradiance estimated from a combination of ^{10}Be and ^{14}C records (Steinhilber et al., 2012), and (f) $\Delta^{14}C$ measured in tree rings (Reimer et al., 2013). The yellow bars indicate intervals of good correlation.

3. 北冰洋加拿大盆地的年龄：来自高分辨率磁异常数据的约束

翻译人：李园洁 liyj3@sustech.edu.cn

Zhang T, Dyment J, Gao J Y. ***Age of the Canada Basin, Arctic Ocean: indications from high-resolution magnetic data****[J].* ***Geophysical Research Letters****, 2019. Doi.: 10.1029/2019GL085736.*

摘要：美亚海盆的起源和历史过程长期存在争议，这阻碍了人们对北极中生代构造背景和地球动力学过程的认识。这种认识的缺乏部分是由于冰覆盖盆地缺乏准确的磁数据所引起的。本文，我们通过高分辨率深拖和海平面观测的磁数据，确定出美亚海盆主要部分-加拿大盆地的地壳年龄。由高分辨率磁异常数据显示的四对磁异常条带的最佳吻合年龄为 139.5-128.6Ma（或 142.4-132.8Ma，取决于不同 GPTS）。地壳年龄为外圈北极构造特征的演化提供了关键的约束，并支持这样的假说，即美亚海盆的开启与南阿努伊大洋关闭期间的俯冲有关。

ABSTRACT：The origin and history of the Amerasia basin are long-running debates, which hinder our knowledge of the Mesozoic tectonic configurations and geodynamic processes in the Arctic. This lack of knowledge is due in part to the paucity of accurate magnetic data in the ice-covered basin. Here, we identify the crustal age of the Canada Basin, a major part of the Amerasia Basin, through high-resolution deep-tow and sea surface magnetic data. The best fit of the four pairs of magnetic lineations revealed by the high-resolution magnetic datais139.5-128.6Ma (or 142.4-132.8Ma, depending on the GPTS). The crustal age provides crucial constraints on the evolution nof the circum-Arctic tectonic featuresand generally supports the hypothesisthatthe opening of the Amerasia Basinisrelated to the subductions during the closure of the South Anyui Ocean.

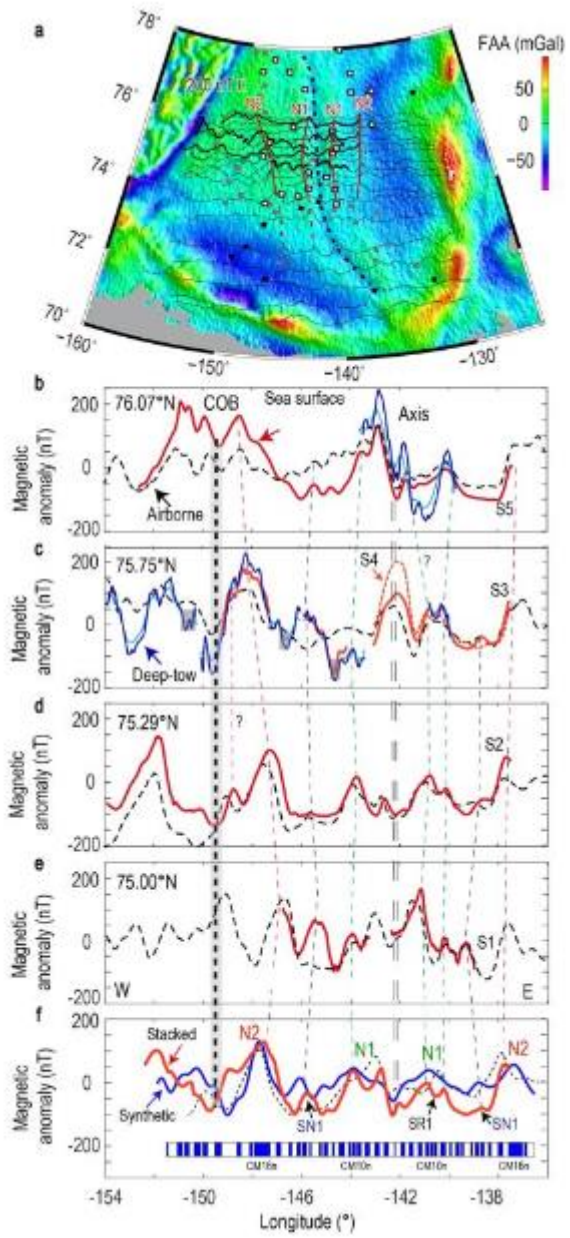

Figure 1. Deep-tow and sea surface magnetic anomalies in the Canada Basin. (a)Deep-tow, sea surface, and airborne magnetic anomalies along their tracks. The background is based on the satellite-derived free air anomaly data [Sandwell et al. 2014]. The continental, transitional, and oceanic crust identified from sonobuoy data [Chian et al., 2016] are shown in black, gray, and white squares, respectively. The relict ridge axis is marked with a dashed line. (b-e) Deep-tow, sea surface, and airborne magnetic anomalies at different latitudes. The upward continued deep-tow data to sea surface andto2000 m below sea surface are shown in light blue and blue, respectively. The sea surface and airborne magnetic data are shown in red and black, respectively. The data associated with diurnal variation > 50 nT are marked with gray boxes. No reduction to the pole is necessary, as the data are collected at high latitude. (f)Stacked sea surface(red), stacked airborne(black), and best-fitting synthetic(blue)magnetic anomalies. The consistent magnetic anomalies between profiles are linked with dashed lines. The magnetic bodies in MHTC12[Malinverno et al., 2012] that produce the synthetic magnetic anomaly at the depth of basement are also shown.

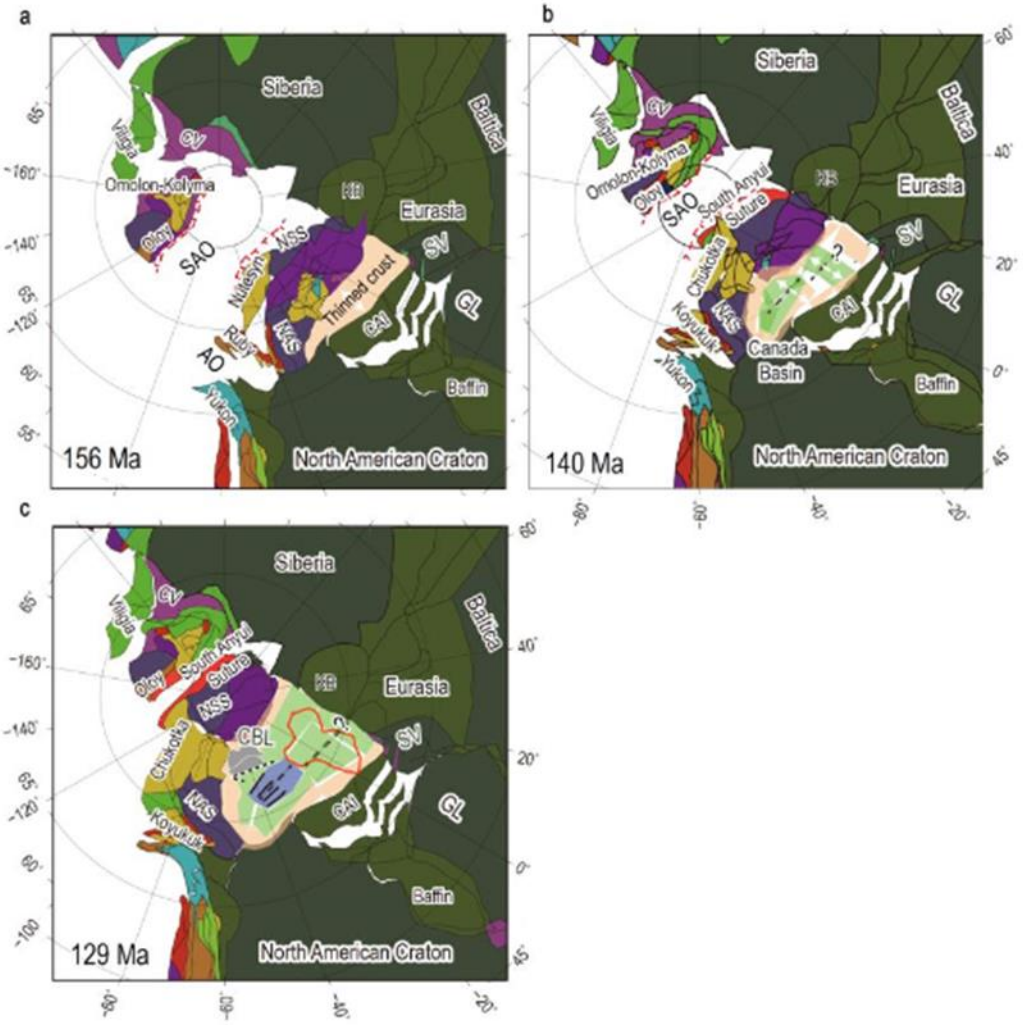

Figure 2. Plate reconstructions of the circum-Arctic region between 156Ma and 129 Ma. The shapes of the geological features are based on Müller et al. [2016]. (a)Rifting created the Amerasia Basin. The South Anyui Ocean was then subducting to the south and north. East of the SAO, the Angayucham Ocean (AO) and associated Koyukuk Arc (initiated at ~160-145 Ma) are believed to be the eastern extensions or the counterparts of the SAO and Nutesyn Arc [Amato,2004,2015; Churkin et al., 1981; Nokleberg et al.,2000], respectively. (b)Initial seafloor spreading in the Amerasia Basin. (c) Seafloor spreading cessation in the Amerasia Basin. The position of the future Alpha Ridge is marked by a red line. Since the position and geometry of the Chukchi Borderland (CBL) in Mesozoic remain controversial [Grantz et al.,1998; Hutchinson et al.,2017; Miller et al., 2006], we only place the CBL in (c)according to its present configuration. The rifting direction in strike-slip models is shown in dashed arrow along the eastern boundary of the Northwind Ridge [Døssing et al., 2018; Hutchinson et al., 2017]. Note the northeast-trending strikeslip is sub-parallel to the subduction zones in the SAO, which may require a new explanation about the dynamic relationship between them. The inferred thinned continental crust, transitional crust, and oceanic crust in the Canada Basin are marked with brown, green, and blue, respectively. Abbreviations:GL, Greenland; SV, Svalbard; KB, Kara Block; NAS, North Alaska Slope; NSS, Northern Siberia Shelf; CV, Central Verkhoyansk.

4. 岁差调控过去一百万年来南太平洋西风带变化

翻译人：仲义 zhongy@sustech.edu.cn

Frank Lamy, John C. H. Chiang, Gema Martinez-Mendez et al., ***Precession modulation of the South Pacific westerly wind belt over the past million years*** *[J].* ***Proceedings of the National Academy of Sciences of the United State****, 2019, https:// doi. Org/10.1073/pnas.1905847116.*

摘要：南部西风带（SWW）连接南极绕极水（ACC）,并强烈地控制着南大洋的碳收支。我们调查过去百万年来阿塔卡马沙漠南部边缘的西南太平洋地区堆积输送量显示出强烈的岁差周期（19/23-ka）。我们使用 2 个海洋-大气环流模型进行模拟表明，观测到的周期性降水变化与水汽从热带太平洋向阿塔卡马沙漠南部输送的经向移动有关。这些变化反映了岁差调控冬季南太平洋西风急流作用。我们推断当岁差极大值时，由于南太平洋西风急流增强，副热带/亚极地急流增强，而中纬度急流较弱时导致阿塔卡马沙漠南部的降水量增强。相反岁差最低值时，我们认为智力北部的干旱环境与副热带/亚极低急流减少和中纬度急流增强有关。在太平洋南部西风带出现的岁差周期，而在其他盆地缺失的现象说明在南半球轨道尺度变化存在区域的不一致性，与南部西风带冰期-间冰期半球范围内迁移不同。急流的增强是南太平洋地区特有现象，可能会影响冬季混合层深度，中层水形成和南极洲海冰的形成，对于研究全球环流体系和海洋固碳作用具有重要的意义。

ABSTRACT: The southern westerly wind belt (SWW) interacts with the Antarctic Circumpolar Current and strongly impacts the Southern Ocean carbon budget, and Antarctic ice-sheet dynamics across glacial– interglacial cycles. We investigated precipitation-driven sediment input changes to the Southeast Pacific off the southern margin of the Atacama Desert over the past one million years, revealing strong precession (19/23-ka) cycles. Our simulations with 2 ocean-atmosphere general circulation models suggest that observed cyclic rainfall changes are linked to meridional shifts in water vapor transport from the tropical Pacific toward the southern Atacama Desert. These changes reflect a precessional modulation of the split in the austral winter South Pacific jet stream. For precession maxima, we infer significantly enhanced rainfall in the southern Atacama Desert due to a stronger South Pacific split jet with enhanced subtropical/ subpolar jets, and a weaker midlatitude jet. Conversely, we derive dry conditions in northern Chile related to reduced subtropical/ subpolar

jets and an enhanced midlatitude jet for precession minima. The presence of precessional cycles in the Pacific SWW, and lack thereof in other basins, indicate that orbital-scale changes of the SWW were not zonally homogeneous across the Southern Hemisphere, in contrast to the hemispherewide shifts of the SWW suggested for glacial terminations. The strengthening of the jet is unique to the South Pacific realm and might have affected wintercontrolled changes in the mixed layer depth, the formation of intermediate water, and the buildup of sea-ice around Antarctica, with implications for the global overturning circulation and the oceanic storage of atmospheric CO2.

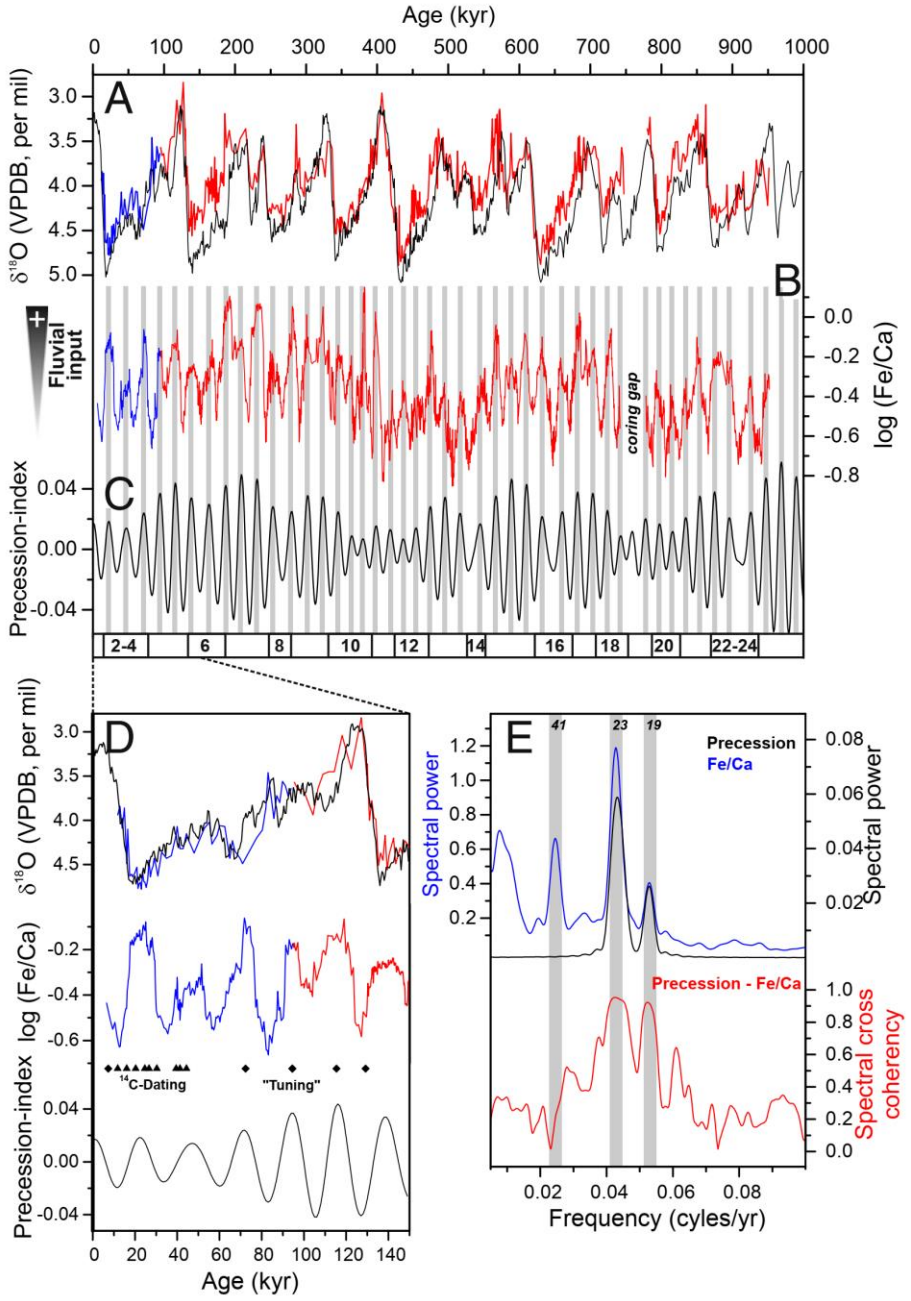

Figure 1. Sedimentological data, stratigraphy, and spectral pattern. (A) Benthic foraminifera oxygen isotope data (blue: core GeoB3375-1, red: GeoB15016) versus LR04 stack (59). (B) log (Fe/Ca)

record documenting changes in fluvial sediment input (SI Appendix, Fig. S2). (C) Precession index. (D) Zoom into last glacial/interglacial cycle with radiocarbon dates and tie points between log (Fe/Ca) and the precession index. Black curve shows intermediate depth Pacific stack (60). (E) Cross-spectral analyses (Blackman–Tukey method; 80% confidence interval) precession versus log (Fe/Ca).

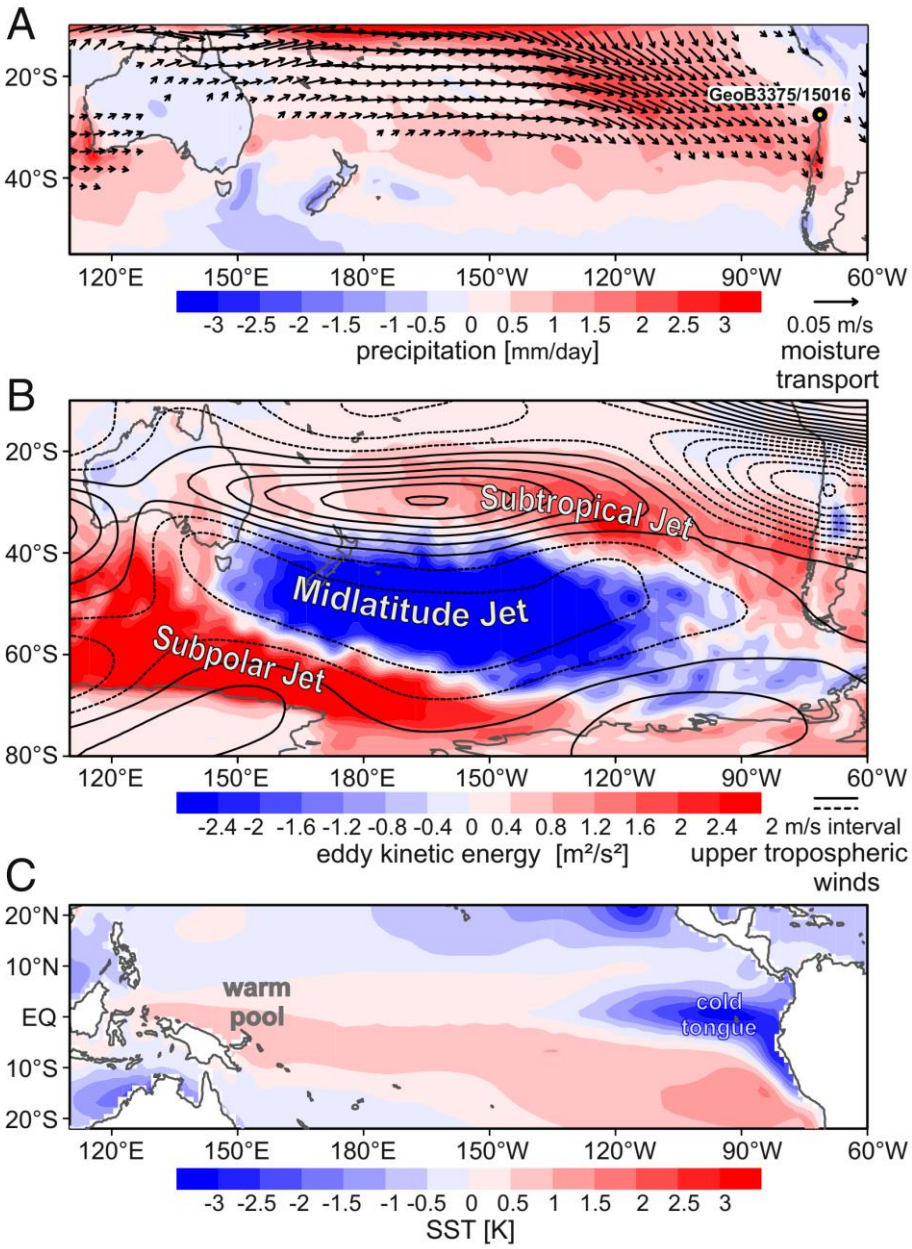

Figure 2. Simulated June–August climate changes resulting from opposite phases of precession, maximum minus minimum. Shown are the results for ECEarth; the equivalent figures for GFDL CM2.1 are shown in SI Appendix, Fig. S6. June–August averages are shown as those are the months of maximum precipitation over subtropical Chile in the simulation. (A) Precipitation (shaded; units are mm/d) and 850-mb moisture transport (wind speed and direction qv; reference vector is 0.05 m/s). For clarity, vectors with zonal components less than +0.005 m/s are not shown. The circle marks the location of the sediment cores. The figure shows increased moisture transport from the central tropical Pacific to subtropical Chile, leading to increases in rainfall there. (B) Upper

tropospheric winds (200 mb; contour interval 2 m/s) and 2–8-d filtered eddy kinetic energy (shaded; units are m2/s2). The latter field is a measure of synoptic eddy activity or "storminess;" we highlight the increased storminess over the southeastern tropical Pacific, coincident with the increased moisture transport and rainfall to subtropical Chile, (C) SST (shaded; units are K). In B, the approximate locations of the climatological subtropical, midlatitude, and subpolar jets are labeled; and in C, the locations of the climatological cold tongue and warm pool regions.

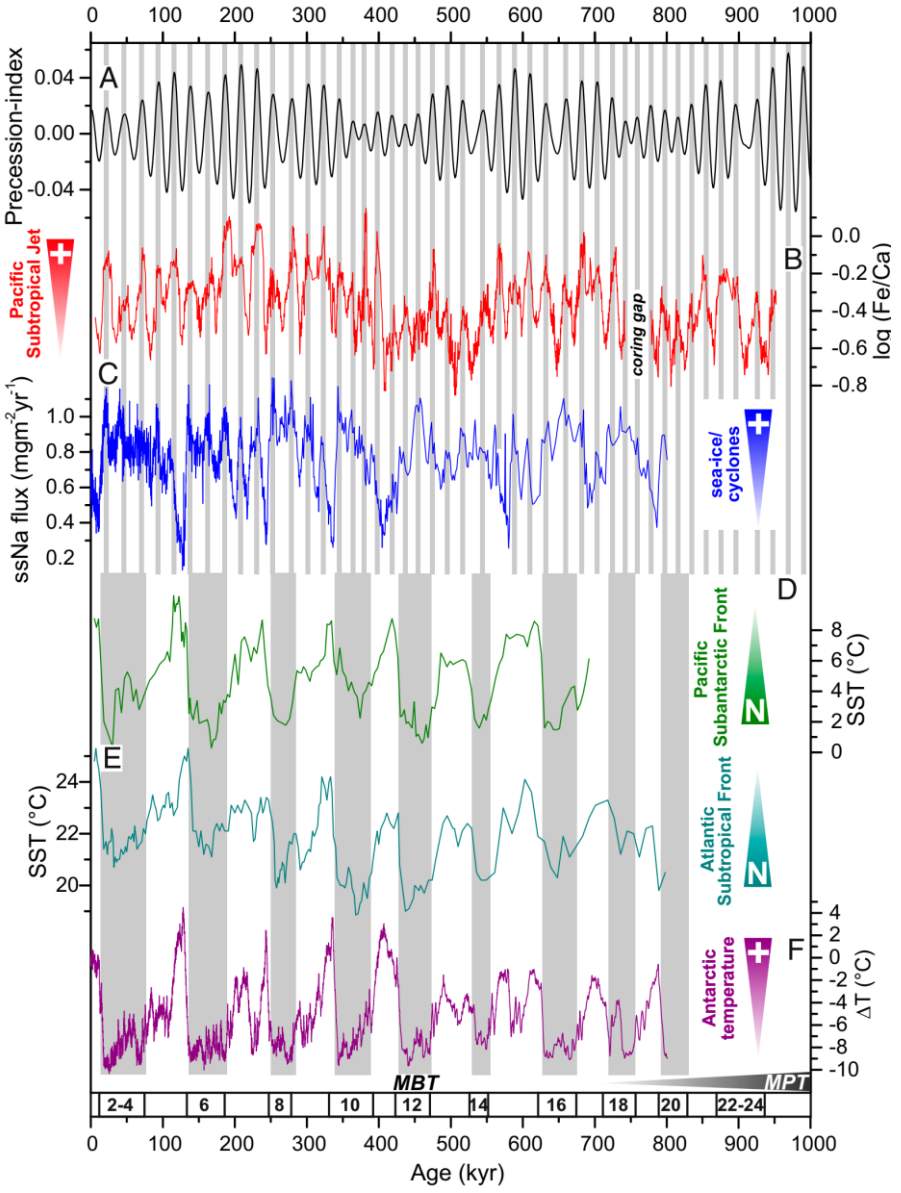

Figure 3. Comparison to other SWW-related records. (A) Precession index. (B) log (Fe/Ca) record as a proxy for changes in the strength of the Pacific STJ. (C) ssNa flux record of the EDC ice core (53, 61). (D) Southeast Pacific SST changes (PS75/34) indicating shifts in the subantarctic front and the midlatitude SWW (23). (E) SST south of SE Africa (MD96/2077) documenting variations in the subtropical front in the western Indian Ocean/ Atlantic (22). (F) Temperature record of the EDC ice core (62). Gray bars across A–C mark precession maxima (reduced austral winter and higher austral summer insolation); Gray bars across D–F mark glacial marine isotope stages numbered below; MBT = Mid-Brunhes Event; MPT = Middle Pleistocene Transition.

5. 南极陆架沉积物与乔治国王岛的铁循环与铁稳定同位素分馏

翻译人：蒋晓东 jiangxd@sustech.edu.cn

Henkel, S., Kasten, S., Hartmann, J. F. et al. ***Iron cycling and stable Fe isotope fractionation in Antarctic shelf sediments, King George Island*** *[J].* ***Geochimica et Cosmochimica Acta*** *(2018), 237, 320-338.*

摘要：来自还原环境沉积物和冰川下沉积物的铁流通量是南大洋生物可利用铁的源区。铁稳定同位素（$\delta^{56}Fe$）被认为是追踪铁源区和反应路径的指标。但由于数据的缺乏和复杂环境下铁循环并未有充分理解，因此对不同类型沉积物，环境条件和生物地球化学过程都缺乏对 $\delta^{56}Fe$ 代表性端元限定。

本研究选定波特湾（受快速冰川撤退影响）的两个取样点（乔治国王岛和南极半岛）测定了孔隙水和沉积物相的 $\delta^{56}Fe$。与无冰区的沉积物相比，靠近冰川前缘的的沉积物含有可还原铁氧化物和黄铁矿，在该区大量表面氧化的冰融水输入到海湾。靠近冰川前缘沉积物中的黄铁矿主要来自于剥蚀的基岩。我们认为靠近冰川的大量可还原铁氧化物主要来自下冰川，该处冰川下物理风化释放的铁与化学风化释放耦合（例如黄铁矿氧化和异化铁还原）。冰川来源的沉积物中高反应性铁池呈现出显著的负 $\delta^{56}Fe$ 信号，并且在该区保持稳定。这表明原位的异化铁还原并未显著改变铁氧化物的铁同位素组成。尽管如此，还原铁氧化物呈现的轻 $\delta^{56}Fe$ 信号表明在还原环境的冰川下物质沉积前发生了潜在微生物铁循环。受氧化冰融水输入影响的沉积物中，孔隙水与反应性铁氧化物呈现强烈的 $\delta^{56}Fe$ 亏损。代表性的研究区反映出密集的氧化还原带和原位铁循环的孔隙水 $\delta^{56}Fe$ 剖面。

本研究表明并不是直接用孔隙水 $\delta^{56}Fe$ 来指示水底铁流通量，因为陆架沉积物的 $\delta^{56}Fe$ 在小的空间上存在大尺度的变化。控制因素是多样的，包括可还原铁氧化物与有机质的量和反应性，以及主要的和次一级含铁物质的同位素组成，还有沉积速率和物理改造（生物扰动和冰川刮蚀）。在冰川下环境调查生物地球化学风化与铁循环时，$\delta^{56}Fe$ 的地球化学具有应用价值。但这要求同位素端元在空间与时间的变化是已知的。由于冰川下环境的地球化学数据有限，为充分评估冰川区及其物质输出区的铁循环和分馏，深入研究 $\delta^{56}Fe$ 分馏是必须的。

ABSTRACT： The Pacific hosts the largest oxygen minimum zones (OMZs) in the world ocean, which Iron (Fe) fluxes from reducing sediments and subglacial environments are potential sources

of bioavailable Fe into the Southern Ocean. Stable Fe isotopes (δ56Fe) are considered a proxy for Fe sources and reaction pathways, but respective data are scarce and Fe cycling in complex natural environments is not understood sufficiently to constrain respective δ56Fe ‘‘endmembers” for different types of sediments, environmental conditions, and biogeochemical processes. We present δ56Fe data from pore waters and sequentially extracted sedimentary Fe phases of two contrasting sites in Potter Cove (King George Island, Antarctic Peninsula), a bay that is affected by fast glacier retreat. Sediments close to the glacier front contain more easily reducible Fe oxides and pyrite and show a broader ferruginous zone, compared to sediments close to the ice-free coast, where surficial oxic meltwater streams discharge into the bay. Pyrite in sediments close to the glacier front predominantly derives from eroded bedrock. For the high amount of easily reducible Fe oxides proximal to the glacier we suggest mainly subglacial sources, where Fe liberation from comminuted material beneath the glacier is coupled to biogeochemical weathering processes (likely pyrite oxidation or dissimilatory iron reduction, DIR). Our strongest argument for a subglacial source of the highly reactive Fe pool in sediments close to the glacier front is its predominantly negative δ56Fe signature that remains constant over the whole ferruginous zone. This implies in-situ DIR does not significantly alter the stable Fe isotope composition of the accumulated Fe oxides. The nonetheless overall light δ56Fe signature of easily reducible Fe oxides suggests pre-depositional microbial cycling as it occurs in potentially anoxic subglacial environments. The strongest 56Fe-depletion in pore water and most reactive Fe oxides was observed in sediments influenced by oxic meltwater discharge. The respective site showed a condensed redox zonation and a pore water δ56Fe profile typical for in-situ Fe cycling. We demonstrate that the potential of pore water δ56Fe as a proxy for benthic Fe fluxes is not straight-forward due to its large variability in marine shelf sediments at small spatial scales (2.4‰ at the site proximal to oxic meltwater discharge vs. 0.9‰ at the site proximal to the marine glacier terminus, both at 2 cm sediment depth). The controlling factors are multifold and include the amount and reactivity of reducible Fe oxides and organic matter, the isotopic composition of the primary and secondary ferric substrates, sedimentation rates, and physical reworking (bioturbation, ice scraping). The application of δ56Fe geochemistry may prove valuable in investigating biogeochemical weathering and Fe cycling in subglacial environments. This requires, however (similarly to the use of δ56Fe for the quantification of benthic fluxes), that the spatial and temporal variability of the isotopic endmember is known and accounted for. Since

geochemical data from subglacial environments are very limited, further studies are needed in order to sufficiently assess Fe cycling and fractionation at glacier beds and the composition of discharges from those areas.

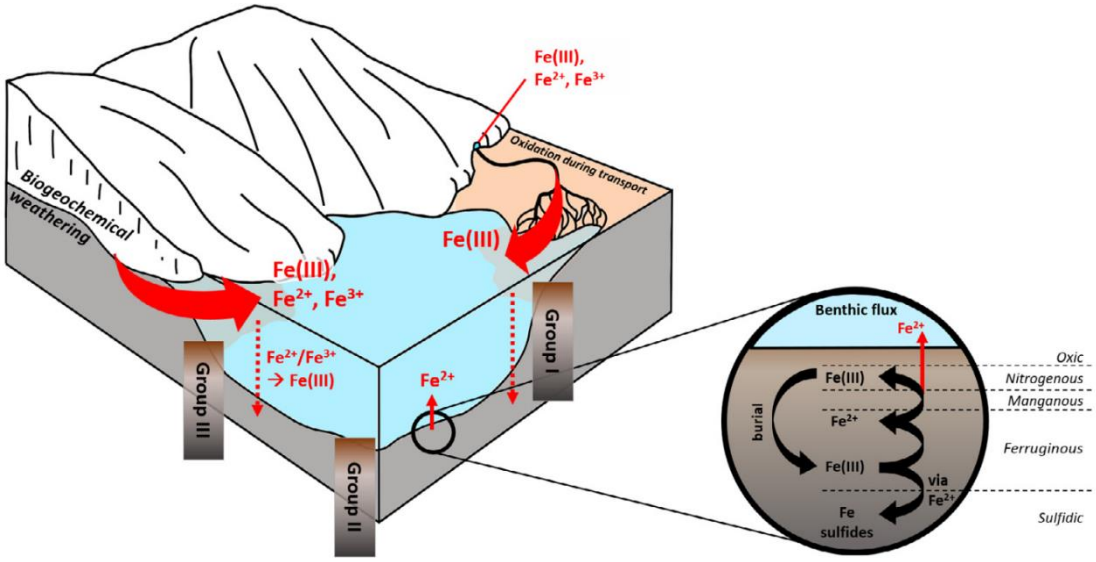

Figure 1. Schematic drawing showing different iron transport and reaction pathways from the glacier to the coastal sea and into marine sediments. The close-up illustrates the early diagenetic redox cycling of Fe in the sediment. Fe^{2+} and Fe^{3+} denote the dissolved, Fe(III) the solid Fe pool. Sediment cores from Potter Cove were classified into Group I, II, and III with regard to their relative location to the glacier terminus and the discharge of surficial meltwater streams as depicted here.

6. 百慕大群岛之下富挥发分转换带

翻译人：冯婉仪 fengwy@sustech.edu.cn

Mazza S E, Gazel E, Bizimis M, et al. ***Sampling the volatile-rich transition zone beneath Bermuda****[J].* ***Nature****, 2019, 569(7756): 398.*

摘要：远离板块边界的板内岩浆省为地幔组成和不均一性提供直接采样的机会。在地幔中观察到的化学不均一性通常归因于俯冲过程中的物质循环，这使得挥发分和不相容元素得以进入地幔。虽然许多板内火山能采集到深部地幔储库（可能在核幔边界）的样品，但不是所有板内火山都具有深部岩浆根，在其他较浅的边界层的储库也可能参与岩浆的形成。在这里，我们提供的证据表明百慕大群岛之下具有一个以前不为人知的地幔域，它以高度富集不相容元素和挥发分的硅不饱和熔体为特征，该熔体具有一个独特的、极端的同位素特征。据我们所知，利用高精度方法得到的数据表明百慕大记录了海盆中最富放射性成因的 $^{206}Pb/^{204}Pb$ 同位素（$^{206}Pb/^{204}Pb$ 比值为 19.9-21.7）。结合低的 $^{207}Pb/^{204}Pb$ 比值（15.5-15.6）和相对不变的 Sr、Nd 和 Hf 同位素，我们认为这个源区的年龄一定小于 6.5 亿年。因此，我们将百慕大源区解释为一个以前不为人知的、短暂的地幔储库，该储库是由于过渡带（在上地幔和下地幔之间）的不相容元素和挥发分的循环和储存导致的，并且只在边界层稳定存在的矿物（如：K-hollandite）中的 Pb 分馏也有利于这种储库的形成。我们认为与泛大陆形成过程中的俯冲事件相关的物质循环进入过渡带是这个储库只在大西洋发现的原因。我们的地球动力学模型表明这个边界层受到地幔流动有关的扰动。地震研究和金刚石包裹体表明循环的物质储存在过渡带。据我们所知，我们首次展示了地球化学证据，证明这种储库是形成极端同位素地幔的关键，而在此之前，人们认为这种地幔只与深部物质循环有关。

ABSTRACT: Intraplate magmatic provinces found away from plate boundaries provide direct sampling of the composition and heterogeneity of the Earth's mantle. The chemical heterogeneities that have been observed in the mantle are usually attributed to recycling during subduction, which allows for the addition of volatiles and incompatible elements into the mantle. Although many intraplate volcanoes sample deep-mantle reservoirs-possibly at the core mantle boundary-not all intraplate volcanoes are deep-rooted, and reservoirs in other, shallower boundary layers are likely to participate in magma generation. Here we present evidence that suggests Bermuda sampled a

previously unknown mantle domain, characterized by silica-undersaturated melts that are substantially enriched in incompatible elements and volatiles, and a unique, extreme isotopic signature. To our knowledge, Bermuda records the most radiogenic $^{206}Pb/^{204}Pb$ isotopes that have been documented in an ocean basin (with $^{206}Pb/^{204}Pb$ ratios of 19.9-21.7) using high-precision methods. Together with low $^{207}Pb/^{204}Pb$ ratios (15.5-15.6) and relatively invariant Sr, Nd, and Hf isotopes, the data suggest that this source must be less than 650 million years old. We therefore interpret the Bermuda source as a previously unknown, transient mantle reservoir that resulted from the recycling and storage of incompatible elements and volatiles in the transition zone (between the upper and lower mantle), aided by the fractionation of lead in a mineral that is stable only in this boundary layer, such as K-hollandite. We suggest that recent recycling into the transition zone, related to subduction events during the formation of Pangea, is the reason why this reservoir has only been found in the Atlantic Ocean. Our geodynamic models suggest that this boundary layer was sampled by disturbances related to mantle flow. Seismic studies and diamond inclusions have shown that recycled materials can be stored in the transition zone. For the first time, to our knowledge, we show geochemical evidence that this storage is key to the generation of extreme isotopic domains that were previously thought to be related only to deep recycling.

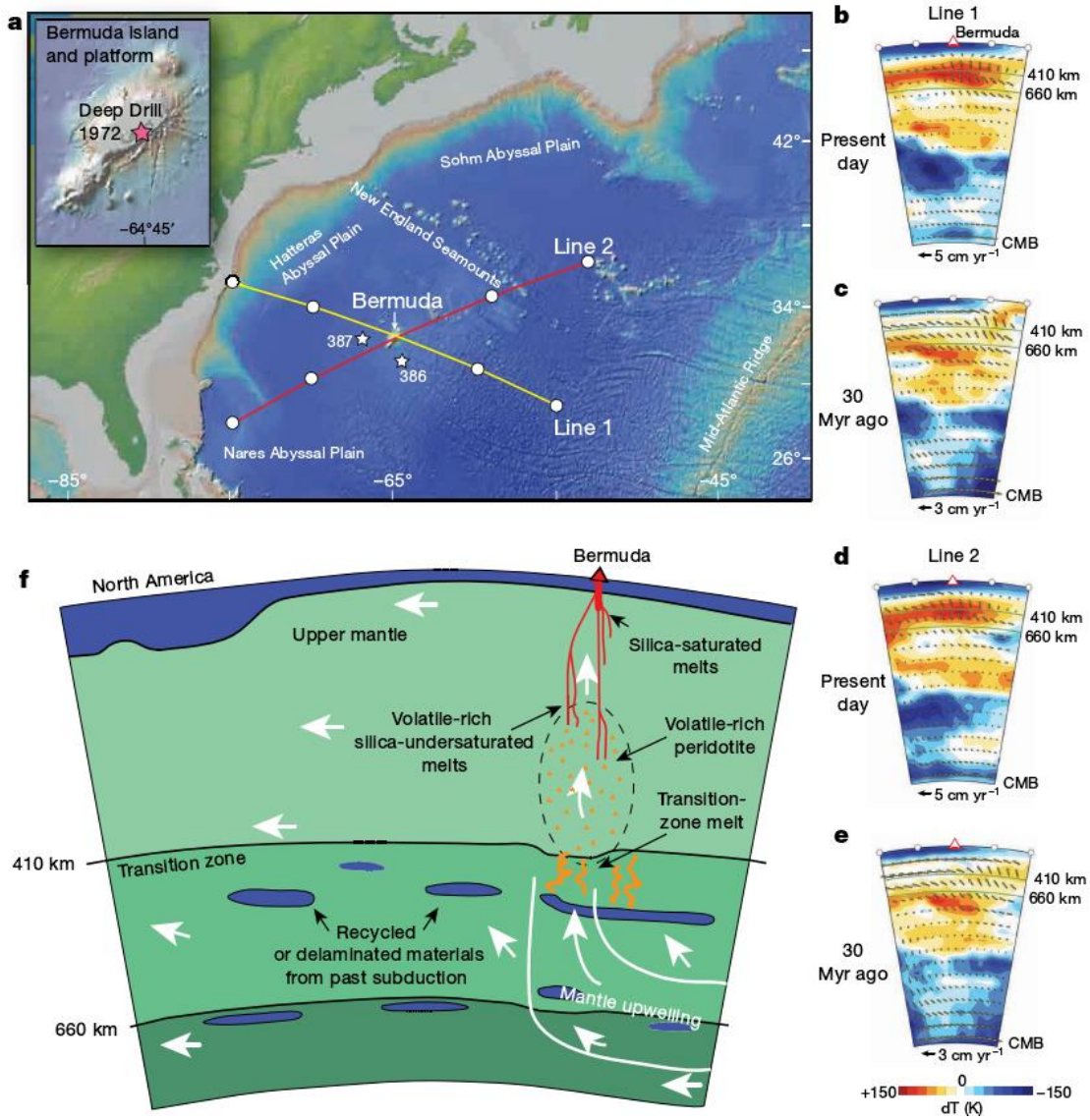

Figure 1. Map, geodynamic and schematic models of Bermuda. a, Map of the Atlantic Ocean indicating the location of Bermuda, the Deep Drill 1972 borehole, and the two cross-sectional lines used for geodynamic modelling, modified from http://www.geomapapp.org 35. b, d, Present-day mantle flow and thermal heterogeneity cross-section, inferred from joint seismic-geodynamic model TX2008 with mantle viscosity V2 following ref. 16, for lines 1 and 2 shown in a. c, e, Corresponding reconstructed mantle flow and thermal heterogeneity at 30 Myr ago using backward advection 16 (note the different flow-velocity scale compared to the present day). f, Schematic model to explain the volcanism of Bermuda as a product of small convection in the upper mantle. White lines and arrows represent mantle flow as modelled by b-e, which samples both the volatile-rich peridotite and the depleted upper mantle. Depressions at 410 km and 660 km are not drawn to scale, but approximate previous observations 14. Recycled material at the base of the transition zone represents trapped subducted crust from previous models 34. CMB, core-mantle boundary.

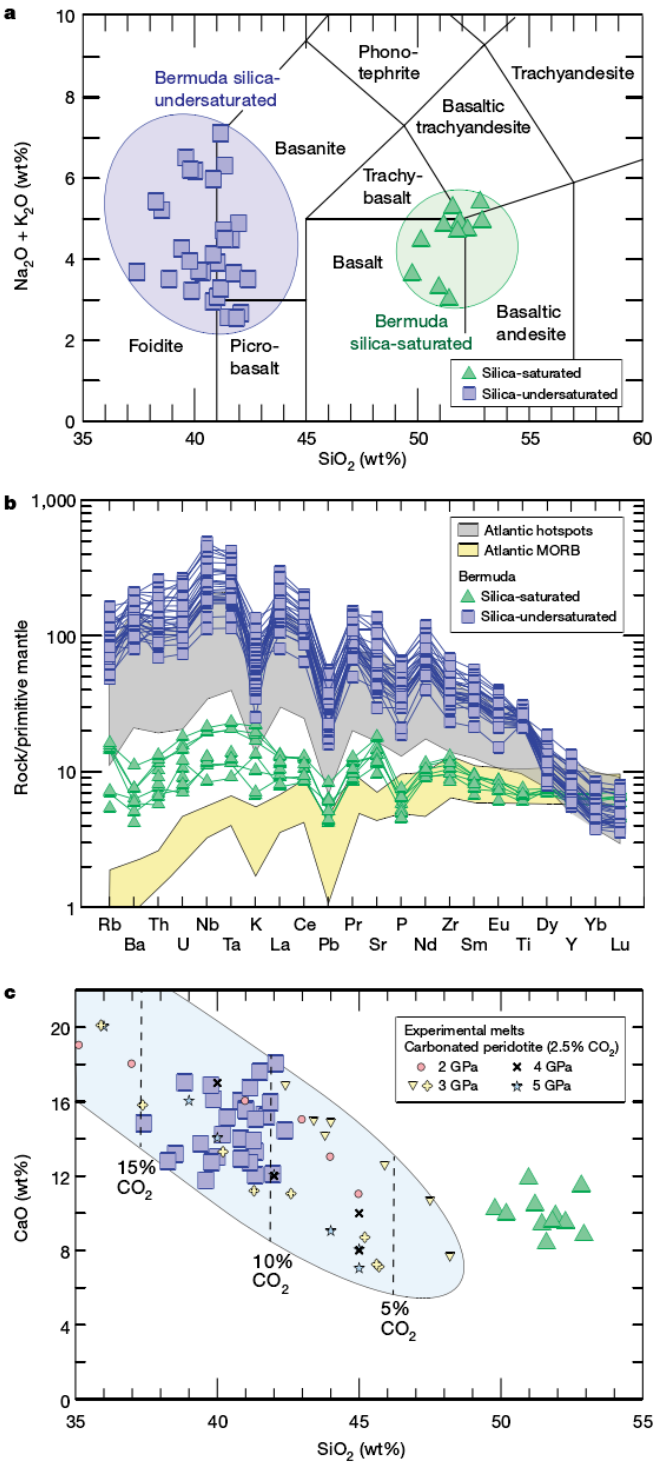

Figure 2. Bulk rock geochemistry of Bermuda. a, Total alkali content ($Na_2O + K_2O$) plotted against SiO_2 content (in weight per cent). Regions containing silica-undersaturated and silica-saturated rocks are shaded in blue and green, respectively. b, Normalized trace element abundances in the primitive mantle for Bermuda, Atlantic mid-ocean-ridge basalt (MORB) (23°-33° N) and Atlantic hotspots from the Geochemistry of Rocks of the Oceans and Continents (GEOROC) database. c, Comparison of the CaO and SiO_2 contents (in weight per cent) of Bermuda with experimental data from melting carbonated peridotite and eclogite [22,23]. The blue shaded region contains experimental melts from a carbonated source, and the dashed lines indicate the stated percentage of CO_2 in the primary melts.

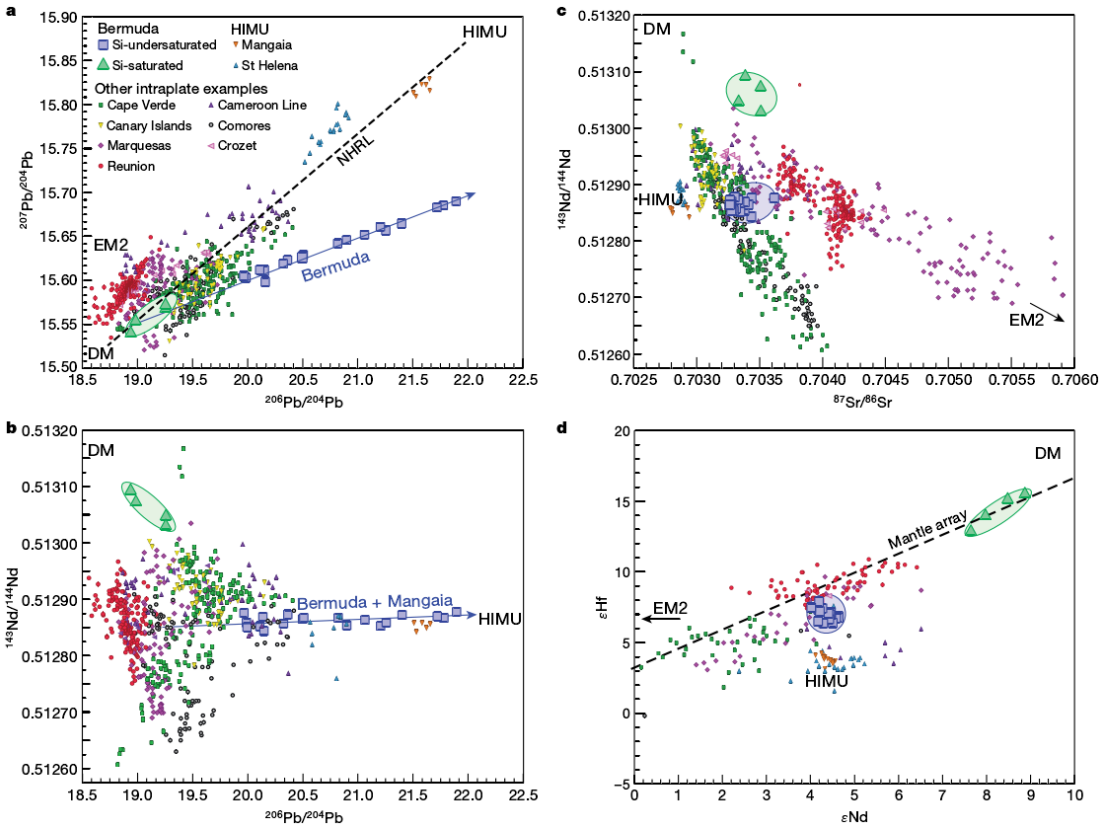

Figure 3. Pb, Sr, Nd and Hf isotopic composition of Bermuda lavas. Radiogenic isotopes for Bermuda compared with Mangaia, St Helena, Cape Verde, Cameroon Line, Canary Islands, Marquesas, Crozet, Comores and Reunion ocean island basalts. The data were obtained from the GEOROC database; Mangaia samples were limited to analyses obtained via multicollector inductively coupled plasma coupled to mass spectrometry. a, $^{207}Pb/^{204}Pb$ plotted against $^{206}Pb/^{204}Pb$, showing a shallow slope for Bermuda silica-undersaturated samples, with $^{206}Pb/^{204}Pb$ similar to that of Mangaia and St Helena. b, $^{143}Nd/^{144}Nd$ plotted against $^{206}Pb/^{204}Pb$, showing invariable $^{143}Nd/^{144}Nd$ in the silica-undersaturated samples with $^{206}Pb/^{204}Pb$ more radiogenic than Mangaia. c, $^{143}Nd/^{144}Nd$ plotted against $^{87}Sr/^{88}Sr$, showing near-consistent $^{87}Sr/^{88}Sr$ for Bermuda with Bermuda silica-saturated having more radiogenic Nd. d, εHf against εNd showing Bermuda silica-undersaturated samples, plotting close below the mantle array. Regions containing silica-undersaturated and silica-saturated rocks are shaded in blue and green, respectively. DM, depleted mantle; EM2, enriched mantle 2; NHRL, Northern Hemisphere reference line.

7. 十万年来的地磁场演化

翻译人：柳加波 liujiabo7@gmail.com

Panovska S, Korte M, Constable C G. ***One hundred thousand years of geomagnetic field evolution****[J].* ***Reviews of Geophysics****, 2019.*

摘要：来自沉积物，考古文物和熔岩流的古磁记录为研究 0-100 ka 的古地磁场变化提供了基础。在晚第四纪 0-100 ka 之间，随着时间变化的球谐模型提供了一个全局视图，该全局视图被用于评估新的数据记录，研究百年至几千年时间尺度上的古地磁长期变化，并研究极端的区域或全球事件，例如 Laschamp 地磁漂移。最近的建模结果（GGF100k 和 LSMOD.2）比较了以前基于区域或全球的相对地磁古强度的 stacks 和平均的变化研究。时间平均的地磁场结构在全新世，100ka 和百万年的尺度上是相似的。古地磁在 0-100 ka 之间的变化非常显著，地磁场强度和地磁场的形态都有非常大的改变，尤其是在地磁场强度较弱的时候。在全球性的地磁漂移事件中，地磁场模型 GGF100k 在地磁轴向偶极矩中表现出 4 倍的变化，而更高分辨率的模型表明可能会有更大的变化。有一些证据表明类似于现今南大西洋地磁异常的状态经常发生，但这些状态与漂移的开始或演化无关。用来表征“Earth-like”发电机数值模拟的多个特征被评估，并且在将来，改进的模型可能仍会揭示与地磁漂移事件发生有关的系统变化。模拟结果有着广泛的应用，在从地动学模拟中的地面实况数据和数据同化，到提供地质年代学约束，以及模拟地磁变化对宇宙核素生产率的影响。

ABSTRACT： Paleomagnetic records from sediments, archeological artifacts, and lava flows provide the foundation for studying geomagnetic field changes over 0-100 ka. Late Quaternary time-varying spherical harmonic models for 0--100 ka produce a global view used to evaluate new data records, study the paleomagnetic secular variation on centennial to multi-millennial timescales, and investigate extreme regional or global events such as the Laschamp geomagnetic excursion. Recent modeling results (GGF100k and LSMOD.2) are compared to previous studies based on regional or global stacks and averages of relative geomagnetic paleointensity variations. Time-averaged field structure is similar on Holocene, 100 ky, and million-year timescales. Paleosecular variation activity varies greatly over 0-100 ka, with large changes in field strength and significant morphological changes that are especially evident when field strength is low. GGF100k exhibits a factor of 4

variation in geomagnetic axial-dipole moment, and higher resolution models suggest much larger changes are likely during global excursions. There is some suggestion of recurrent field states resembling the present day South Atlantic Anomaly, but these are not linked to initiation or evolution of excursions. Several properties used to characterize numerical dynamo simulations as ``Earth-like'' are evaluated and, in future, improved models may yet reveal systematic changes linked to the onset of geomagnetic excursions. Modeling results are useful in applications ranging from ground truth and data assimilation in geodynamo simulations to providing geochronological constraints, and modeling the influence of geomagnetic variations on cosmogenic isotope production rates.

8. 俯冲通量调节地磁极性倒转速率

翻译人：杨会会 11849590@mail.sustech.edu.cn

Hounslow M W, Domeier M, Biggin A J. ***Subduction flux modulates the geomagnetic polarity reversal rate[J].Tectonophysics****, 2018: 34–49*

摘要：确定显生宙地磁极性逆转频率变化的原因，一直是古磁学和地球动力学研究的首要课题。很多模型表明在 10-100 Ma 尺度上控制地磁极性倒转的主要因素是核-幔边界上不断变化的热通量，而这个热通量本身强烈地受到俯冲入地幔的岩石圈通量变化的影响。随时间变化的全球俯冲通量与地磁倒转频率之间存在正相关关系，且将热量特征传递到最下层地幔存在时间延迟。我们利用早古生代的俯冲通量估计和地磁换向率数据对这一假设进行了首次检验。俯冲区通量的估算源自全球板块构造模型，计算方法也区别于那些根据碎屑锆石和锶同位素的全球年龄分布计算的独立俯冲通量指标。根据之前可追溯到约 320 Ma 的数据合集和一个新的在数据稀疏的早-中古生代建立的倒转速率模型，本文建立了一个连续的显生宙的倒转速率模型。通过对随时间变化的俯冲通量与地磁倒转速率序列的交叉频谱分析显示两者显著相关，且地磁倒转滞后于俯冲约 120 Ma。这个 120 Ma 的之后代表了一个中间值，介于俯冲板块从地表到核-幔边界的地震约束时间（~ 150-300 Ma）和一些更短的通过地幔流数值模型预测的时间（~ 30-60 Ma）之间。虽然造成这种巨大差异的原因尚不清楚，但令人鼓舞的是我们对滞后时间的估计代表了两者之间的折衷。虽然我们提出的关系中仍存在重要的不确定性，但这些结果为地表与深部地球之间的动态联系提供了新的线索，并将有助于约束连接地幔对流、最下层地幔的热演化和地球发电机的新模型。

ABSTRACT: Ascertaining the cause of variations in the frequency of geomagnetic polarity reversals through the Phanerozoic has remained a primary research question straddling paleomagnetism and geodynamics for decades. Numerical models suggest the primary control on geomagnetic reversal rates on 10 to 100 Ma timescales is the changing heat flux across the core-mantle boundary and that this is itself expected to be strongly influenced by variations in the flux of lithosphere subducted into the mantle. A positive relationship between the time-dependent global subduction flux and magnetic reversal rate is expected, with a time delay to transmit the thermal imprint into the lowermost mantle. We perform the first test of this hypothesis using subduction

flux estimates and geomagnetic reversal rate data back to the early Paleozoic. Subduction area flux estimates are derived from global, full-plate tectonic models, and are evaluated against independent subduction flux proxies based on the global age distribution of detrital zircons and strontium isotopes. A continuous Phanerozoic reversal rate model is built from pre-existing compilations back to ~320 Ma plus a new reversal rate model in the data-sparse mid-to-early Paleozoic. Cross-correlation of the time-dependent subduction flux and geomagnetic reversal rate series reveals a significant correlation with a time delay of ~120 Ma (with reversals trailing the subduction flux). This time delay represents a value intermediate between the seismologically constrained time expected for a subducted slab to transit from the surface to the core-mantle boundary (~150–300 Ma), and the much shorter lag time predicted by some numerical models of mantle flow (~30–60 Ma). While the reason for this large discrepancy remains unclear, it is encouraging that our novel estimate of lag time represents a compromise between them. Although important uncertainties in our proposed relationship remain, these results cast new light on the dynamic connections between the surface and deep Earth, and will help to constrain new models linking mantle convection, the thermal evolution of the lowermost mantle and the geodynamo.

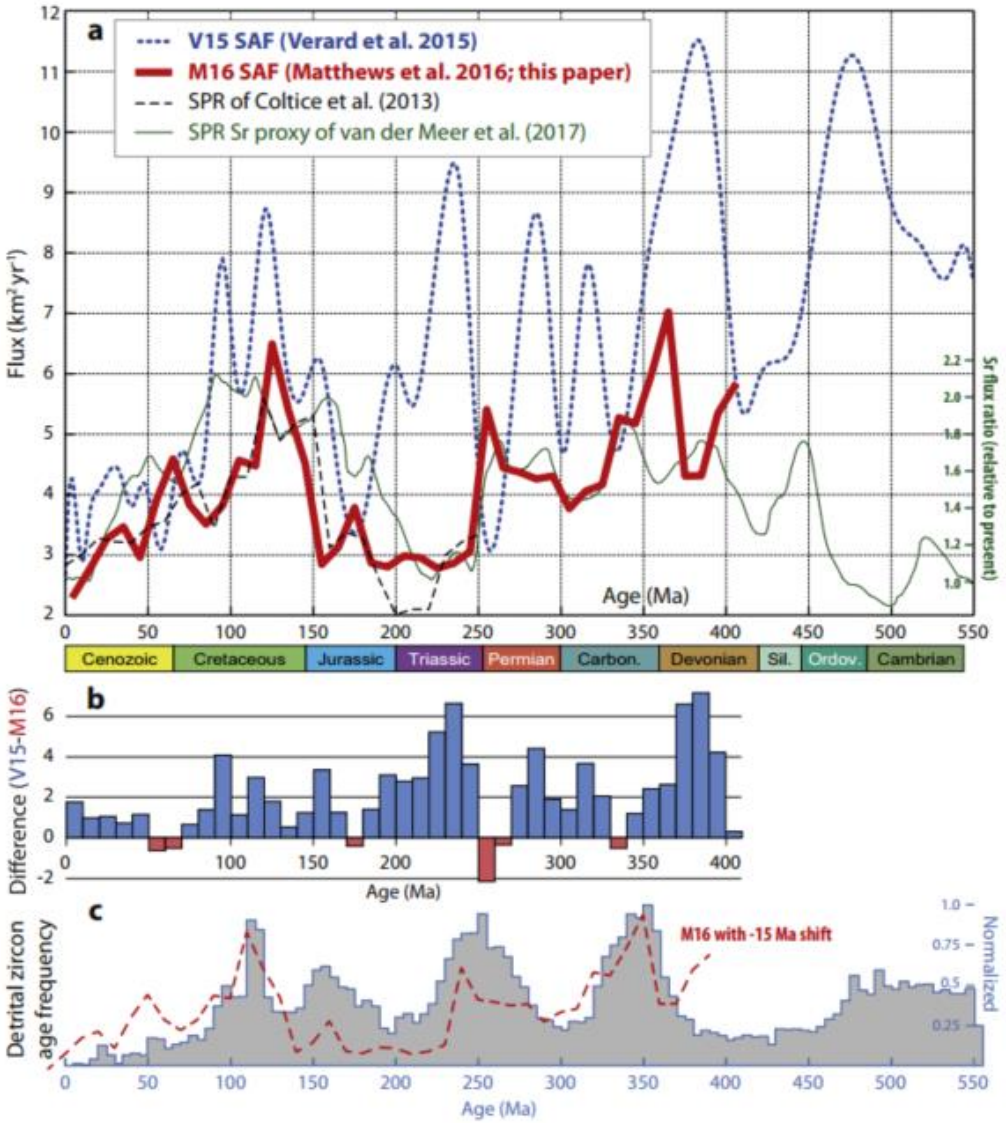

Figure 1. Subduction area flux (SAF) and seafloor production (SPR) rates from previous studies and this work. The V15 SAF was calculated by Vérard et al. (2015), based on the University of Lausanne geodynamic model (now industry owned) that extends back to 600 Ma. The M16 SAF is calculated in this paper, based on the model of Matthews et al.(2016) which extends to 410 Ma (see Supplementary materials). The SPR of Coltice et al. (2013) is derived from the plate model of Seton et al. (2012),extending back to the Early Triassic (250 Ma). The SPR Sr proxy is based on the estimated 'mantle' strontium flux calculated by van der Meer et al.(2017) and extends into the Precambrian. b) The time-dependent differences in estimated flux according to the V15 and M16 models; blue (red) bars highlight those intervals where V15 (M16) report higher rates. c) Normalized detrital zircon age frequency based on the database of Voice et al. (2011); see text for details. Red dashed line shows the M16 SAF for comparison, after a 15 Ma shift applied according to the 'crystallization delay' detailed in the text. (For interpretation of the references to color in this figure legend, the reader is referred to the web version of this article.)

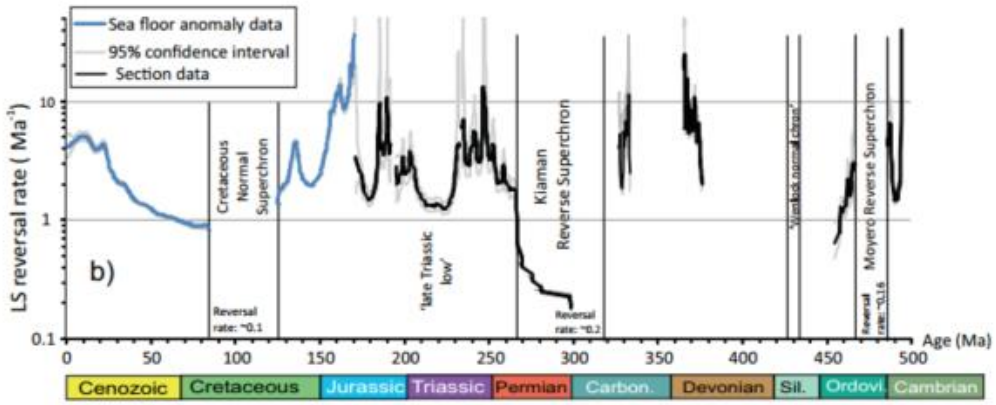

Figure 2. The LS reversal rate data, derived from the LOCFIT estimating procedure, and the 95% confidence intervals on the LS reversal rates (data reported in Supplementary data). The reversal rate frequency during the superchrons is shown, based on known subchrons within the superchrons.

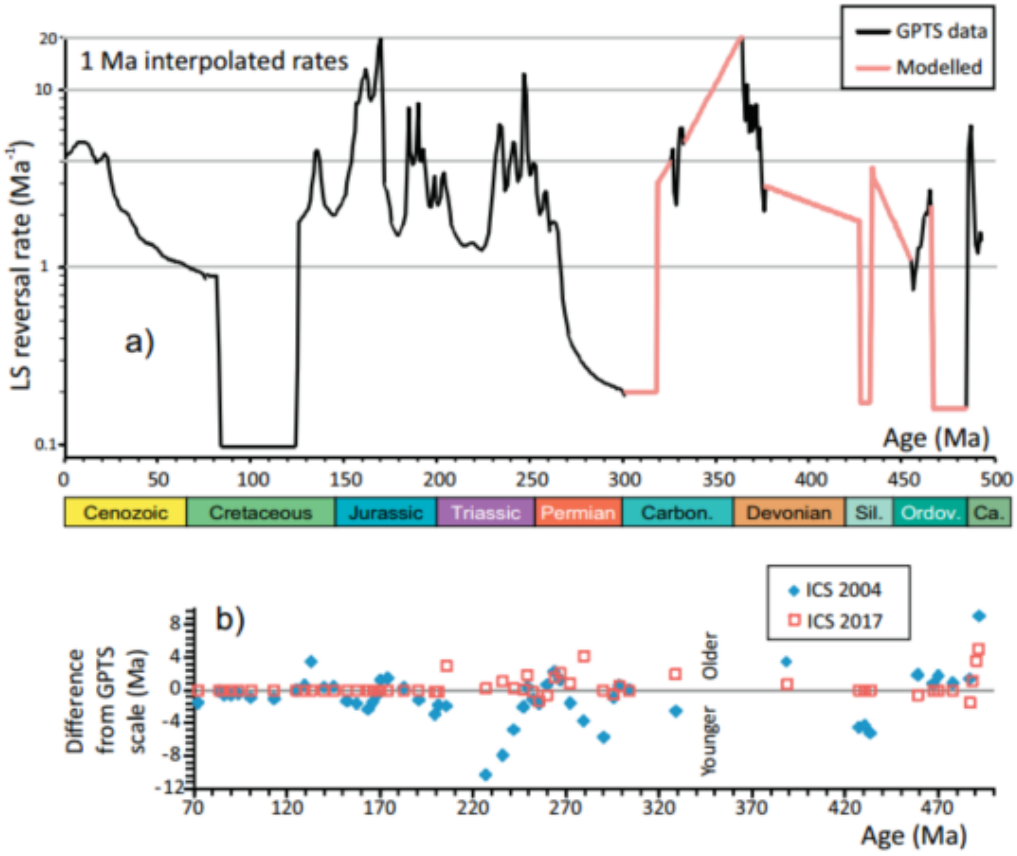

Figure 3. a) The reversal rates at 1 Ma intervals interpolated from the LS reversal rate at each chron, along with the modelled values of reversal rates in the Paleozoic, where data is absent. b) Time offsets from the geomagnetic polarity time scale (i.e. age of stage bases), as used here, to illustrate the likely scale of age offsets between the SAF data and the geomagnetic polarity. Older (younger) ages indicate SAF ages are older (younger) than the GPTS ages used here. ICS 2004 and 2017 are the stage base ages produced by the International Commission on Stratigraphy, which relate largely (but not entirely) to the timescales in Gradstein et al. (2012, 2004). Prior to 70 Ma, differences are small and < 0.5 Ma (not shown).

9. 纳米级针铁矿在红层中是一种重磁化的潜在指示物

翻译人：王浩森 502691781@qq.com

Huang W, Jackson M J, Dekkers M J, et al. ***Nanogoethite as a potential indicator of remagnetization in red beds****[J].* ***Geophysical Research Letters****, 2019.*

摘要：红层能够记录稳定的天然剩磁（NRM），但是如何成功将原生剩磁信息从次生剩磁信息中提取出来一直是红层古地磁研究的难题。青藏高原东部的古近纪红层记录了附近岩浆作用引起的重磁化现象，是进行红层重磁化研究的理想材料。通过系统的岩石磁学、光谱学和岩石相学的分析发现，重磁化过程主要受温度控制。重磁化的红层中含有大量的自生赤铁矿和针铁矿，大颗粒矿物在对应的尼尔温度发生解阻，剩余的小颗粒在较低的温度发生解阻。相反，仍保留有原生剩磁信息的红层样品中，主要的载磁矿物是碎屑赤铁矿和磁铁矿，含有少量的细粒自生赤铁矿，但是不存在自生针铁矿和磁铁矿。 天然剩磁和磁化率的高温结果进一步指示了重磁化现象。但是，自生纳米针铁矿的存在对于重磁化的响应较明显，是判断重磁化红层的敏感指标。

ABSTRACT： Red beds are well-known for recording stable natural remanent magnetization (NRM). However, discriminating primary NRM from secondary remanence in red beds is difficult. The Paleogene Nangqian red beds in eastern Tibetan Plateau variably record an overprint related to nearby magmatism and thus provide a great opportunity to characterize remagnetization in red beds. Through comprehensive rock magnetic, Mössbauer spectroscopic, and petrographic analyses, we find that remagnetization was controlled by temperature. Remagnetized red beds contain abundant authigenic hematite and goethite, with some larger grains unblocking at the Néel temperatures and the remainder (nanoparticles) unblocking at lower temperatures. In contrast, red beds retaining primary NRM are characterized by dominance of detrital hematite and magnetite, presence of fine-grained authigenic hematite, and absence of authigenic goethite and magnetite. High temperature behaviors of NRM/susceptibility are indicative of remagnetization, but the presence of goethite appears to be a more sensitive criterion for diagnosing remagnetization in red beds.

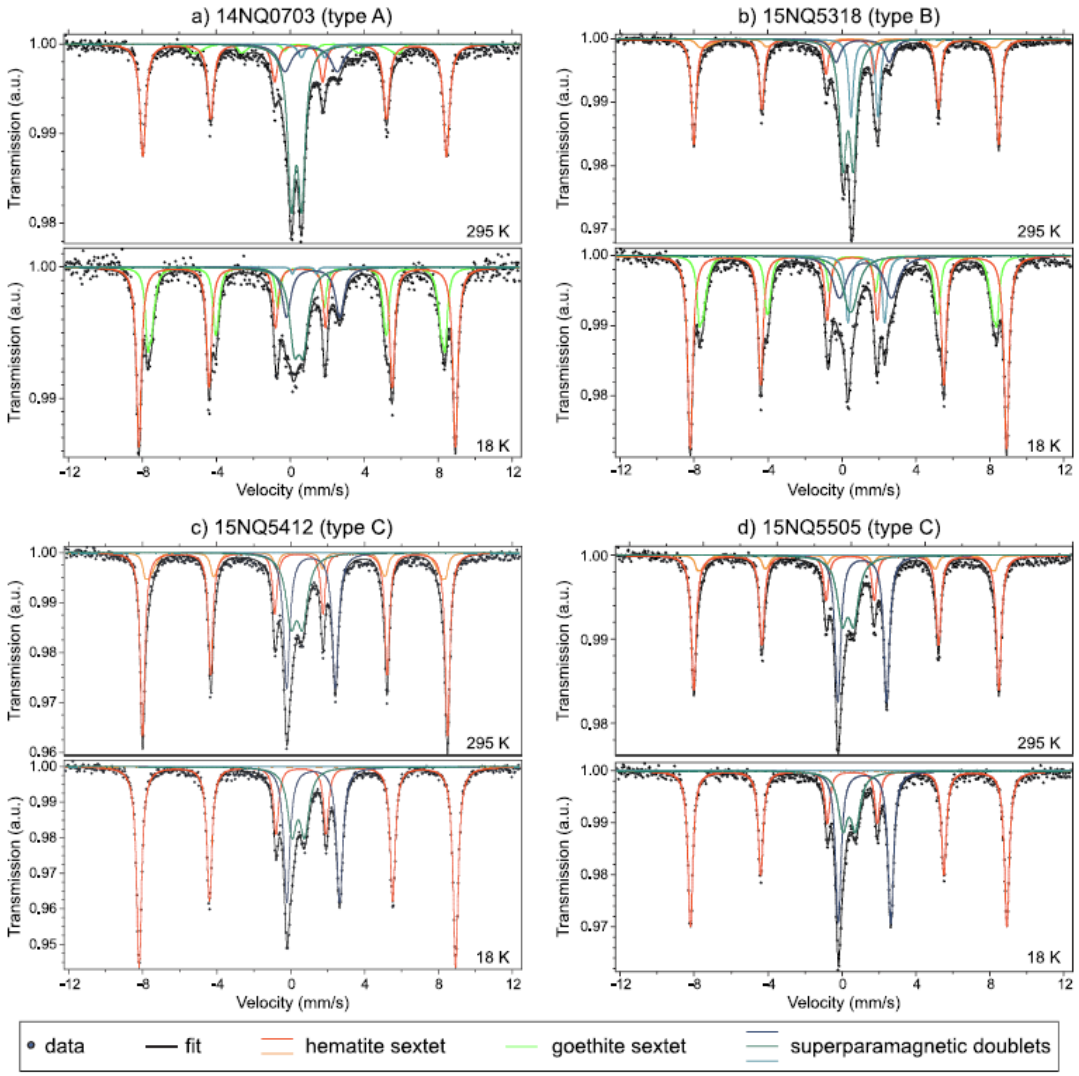

Figure 1. Mössbauer spectrum acquired at 295 and 18 K for powder red bed samples. Dots with the black lines are data and model fits. Red and yellow sextets are the fits diagnostic of hematite; green sextet represents goethite (significant only in Types A and B samples, especially at low temperature). The central peaks comprised superposed doublets dominated by Fe^{3+}.

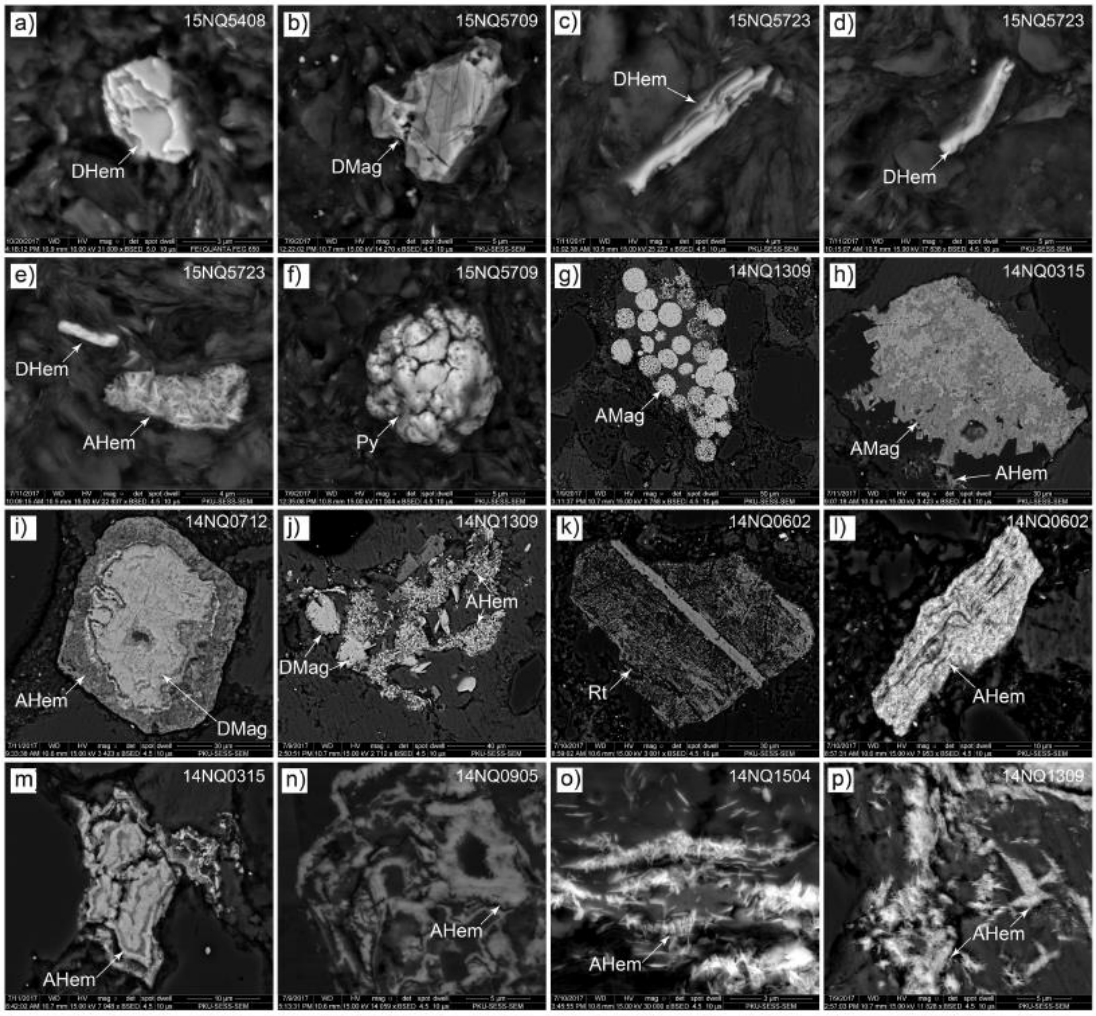

Figure 2. SEM backscattered electron images of samples from the Nangqian red beds (a–f) from Type C samples, (i,o) from Type A samples, and the remainder are from Type B samples. DHem = detrital hematite; AHem = authigenic hematite; DMag = detrital magnetite; AMag = authigenic magnetite; Py = pyrite; Rt = rutile.

10. 冰芯中风尘沉积与浮游生物响应的记录

翻译人：王敦繁 dunfan-w@foxmail.com

Hooper, J., Mayewski, P., Marx, S., Henson, S., Potocki, M., Sneed, S., Saunders, K. M. ***Examining links between dust deposition and phytoplankton response using ice cores****[J].* ***Aeolian Research****, 2019, 36, 45-60.*

摘要：风尘是海洋环境中重要的营养物来源，影响着海洋的初级生产力。海洋生产力增强可导致大气中二氧化碳的下降，并被认为可能是冰川-间冰期气候变化的一个驱动因素。然而，这种联系的规模及其在更短的时间尺度上的发生仍然是不明确的，同时还不清楚的是：是否是风尘铁施肥效应，还是其他机制，如营养物质上升流，是高营养盐低叶绿素(HNLC)海洋区域生产力的主要驱动因素。在这项研究中，我们通过对来自南大西洋(South Georgia Island)和北太平洋(Yukon)冰芯中来自风尘的铁和甲基磺酸(海洋生产力的一种测量方法)的研究，证明了无论在事件还是年度尺度上，生产力都与风尘-铁显著相关。然而，在高分辨率冰芯中测定(风尘)铁肥与生产力之间的关系受到许多高度复杂的因素的影响，我们将对这些因素进行讨论并共同提出未来的研究方向。综上所述，我们的研究表明，由于气候变化和扬尘源地区的人类活动，风生铁通量的变化可能对 HNLC 区海洋生产力产生重要影响，从而可能对碳循环产生潜在影响。

ABSTRACT： Dust is a major source of nutrients to remote ocean environments, influencing primary productivity (PP). Enhanced oceanic PP causes drawdown of atmospheric CO2 and is considered likely to be a driver of climate variability on glacial-interglacial timeframes. However, the scale of this relationship and its operation over shorter timescales remains uncertain, while it is unclear whether dust fertilisation, or other mechanisms, e.g. nutrient upwelling, are the primary driver of PP in high-nutrient low-chlorophyll (HNLC) ocean regions. In this study, we demonstrate, using dust derived Fe and Methanesulfonic acid (a measure of ocean PP) deposition in ice cores from the South Atlantic (South Georgia Island) and North Pacific (Yukon), that PP is significantly correlated with Dust-Fe on both an event and annual scale. However, measuring the relationship between (dust) Fe fertilization and PP in high resolution ice cores is subject to a number of highly complex factors, which are discussed and together used to recommend future research directions.

In conclusion, our research suggests that changes in aeolian Fe flux, due to climate change and human activity in dust source regions, could have significant implications for HNLC ocean PP and, therefore potentially, carbon sequestration.

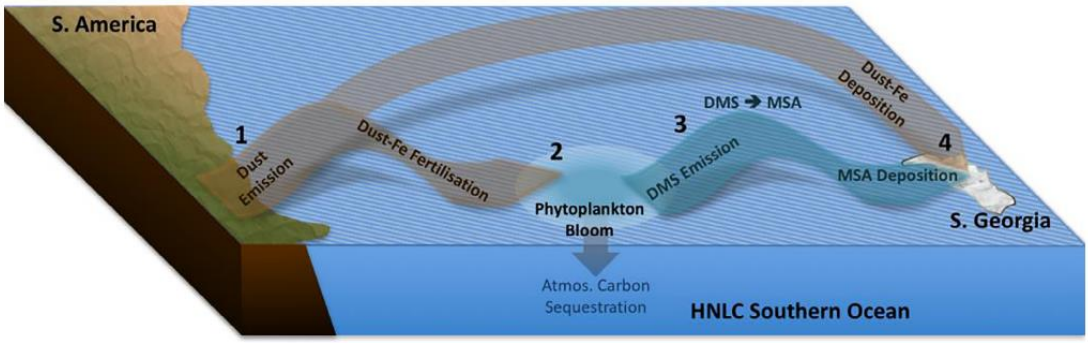

Figure 1. Conceptual diagram illustrating the link between dust deposition, primary productivity (PP) and CO2, and the mechanisms by which temporal variability in this relationship is recorded in ice. The South Atlantic Sector of the Southern Ocean is shown in the diagram by way of example. 1) Dust is emitted from a continental source area and transported in the atmosphere. 2) Dust-Fe is deposited in the HNLC ocean resulting in fertilisation and phytoplankton response. 3) Dimethyl-Sulfide (DMS) is emitted from the phytoplankton bloom and oxidised to become MSA. 4) Methanesulfonic acid (MSA) is transported via the same pathways as Dust-Fe and both are deposited through precipitation on a downwind glacier or ice-cap.

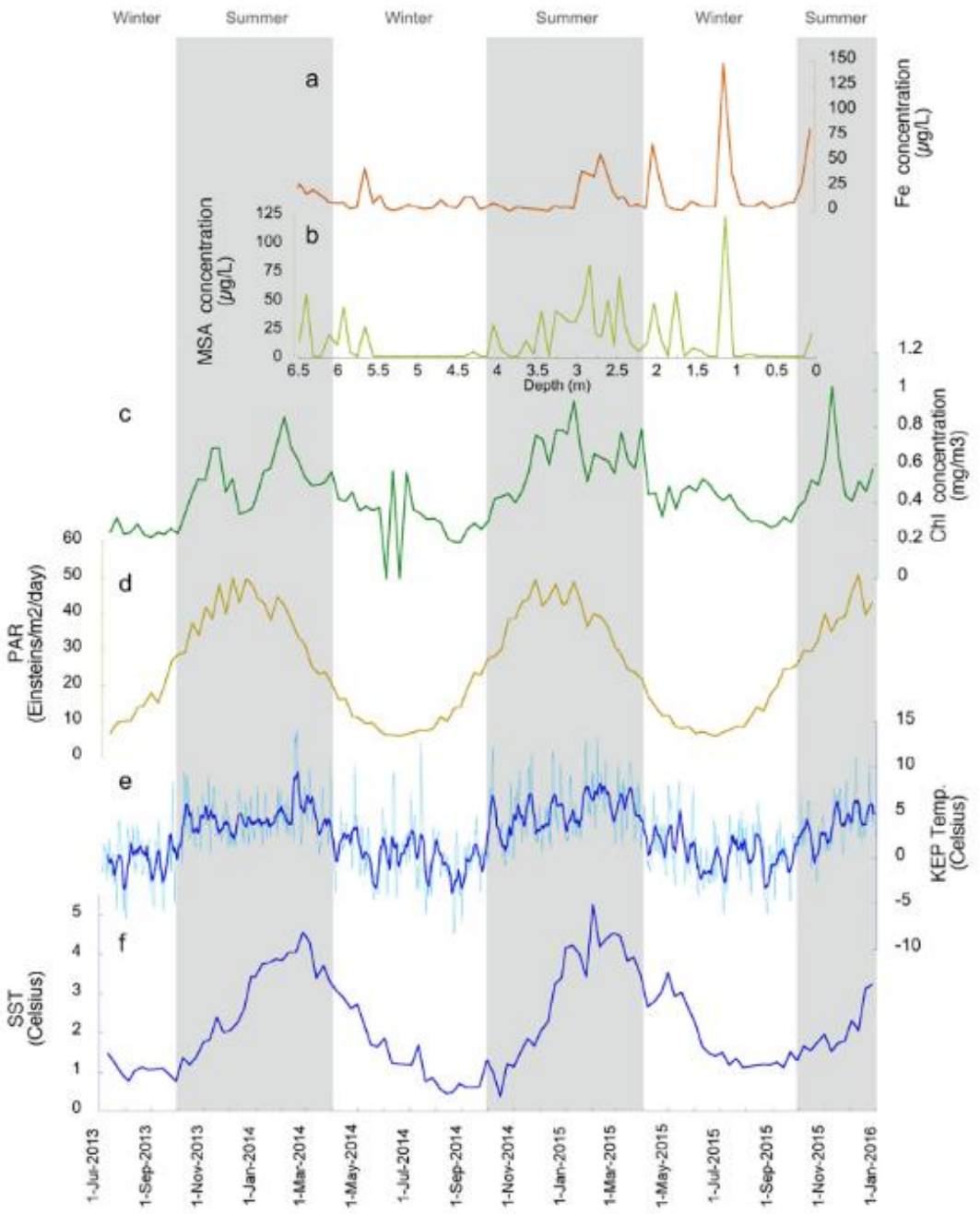

Figure 2. (a) Fe concentrations and (b) MSA concentrations in the South Georgia Core. Zero depth equates to 17th October 2015, the date the core was collected. (c) Average remotelysensed chlorophyll (Chl) concentrations and (d) Average remotely-sensed Photosynthetically Available Radiation (PAR) in the area 51-56° S, 38-48° W upwind of South Georgia. (e) South Georgia, King Edward Point station (KEP) mean daily temperature (light blue), smoothed with an 8-day moving average (dark blue). (f) Average remotely-sensed Sea Surface Temperature (SST) in the area 51–56° S, 38–48° W upwind of South Georgia. (For interpretation of the references to colour in this figure legend, the reader is referred to the web version of this article.)

11. EMAG2：由卫星磁测、航空磁测和海上磁测数据编制的最小分辨率为 2 弧分的地磁异常网格模型

翻译人：曹伟 11930854@mail.sustech.edu.cn

Maus S, Barckhausen U, Berkenbosch H, et al. ***EMAG2: A 2–arc min resolution Earth Magnetic Anomaly Grid compiled from satellite, airborne, and marine magnetic measurements****[J]. **Geochemistry, Geophysics, Geosystems**, 2009, 10(8).*

摘要：全球地磁异常网格模型（EMAG2）是根据卫星磁测、航空磁测和海上磁测数据编制的。EMAG2 是在前期全球数字磁异常图备选网格的基础上做的重要更新。分辨率由 3 弧分提高到 2 弧分，海拔由大地水准面之上 5 公里降低到 4 公里。另外该模型还包括陆地和海洋的网格和轨道线数据。我们尽可能的使用可用的原始船载和航测数据，而不是预先编译的海洋磁网格数据。在海洋地壳年龄模型的基础上，通过定向网格化和外推法改进了海洋稀疏轨迹线之间的插值，由最新的 CHAMP 卫星磁场模型 MF6 替代最长波长（>300km）。EMAG2 可以通过 http://geomag.org/models/EMAG2 获取，相关数据永久存档在 http://earthref.org/ cgi-bin/er.cgi?s=erda.cgi?n=970.

ABSTRACT：A global Earth Magnetic Anomaly Grid (EMAG2) has been compiled from satellite, ship, and airborne magnetic measurements. EMAG2 is a significant update of our previous candidate grid for the World Digital Magnetic Anomaly Map. The resolution has been improved from 3 arc min to 2 arc min, and the altitude has been reduced from 5 km to 4 km above the geoid. Additional grid and track line data have been included, both over land and the oceans. Wherever available, the original shipborne and airborne data were used instead of precompiled oceanic magnetic grids. Interpolation between sparse track lines in the oceans was improved by directional gridding and extrapolation, based on an oceanic crustal age model. The longest wavelengths (>330 km) were replaced with the latest CHAMP satellite magnetic field model MF6. EMAG2 is available at http://geomag.org/models/EMAG2 and for permanent archive at http://earthref.org/ cgi-bin/er.cgi?s=erda.cgi?n=970.

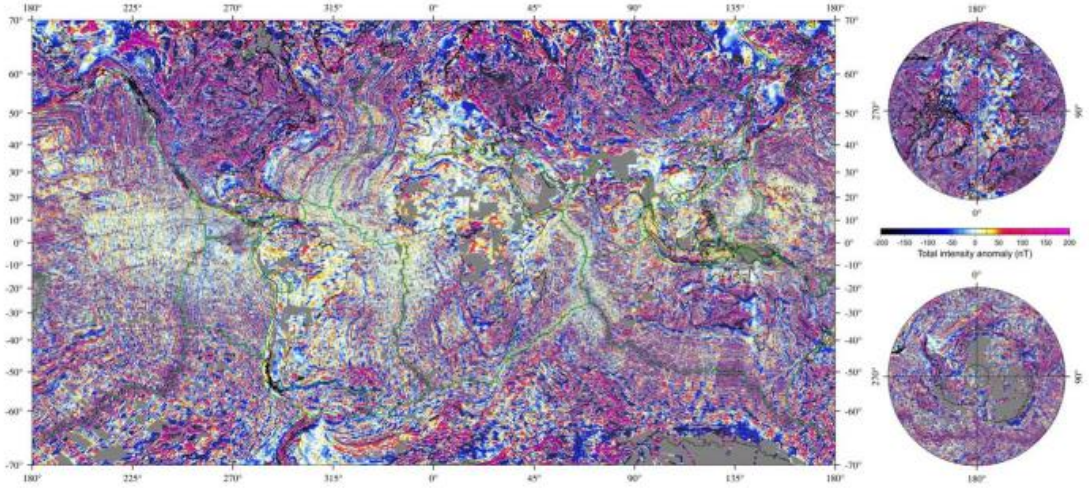

Figure 1. Mercator projection and polar stereographic projections (>40 latitude) of the EMAG2 global grid.

12. 新亚述帝国兴衰的气候视角

翻译人：郑威 11930589@mail.sustech.edu.cn

Sinha A, Kathayat G, Weiss H, et al. ***Role of climate in the rise and fall of the Neo-Assyrian Empire****[J].* ***Science Advances****, 2019, 5(11): eaax6656.*

摘要：伊拉克北部是新亚述帝国（公元前912年-公元前609年）的政治经济中心——是当时最大最具权力的帝国。在统治了当地两个多世纪后，新亚述帝国骤然从它的巅峰时期（公元前670年）走向了它的终点（公元前615年-公元前609年）。早期对亚述帝国崩溃的解释集中关注于国际政治经济冲突、领土过度扩张、和军事失败。文章展示了来自伊拉克北部Kuna Ba Cave高分辨率高精度定年的洞穴石笋样品的气候变化记录，结果显示亚述帝国的兴起发生在过去四千年的背景下的长达两个世纪的气候异常湿润期，然而公元前7世纪早期到中期的巨大干旱严重程度堪比近期的干旱事件，这导致了亚述帝国农业产量严重下滑，因此造成了帝国最终的政治经济崩溃。

ABSTRACT：Northern Iraq was the political and economic center of the Neo-Assyrian Empire (c. 912 to 609 BCE)—the largest and most powerful empire of its time. After more than two centuries of regional dominance, the Neo-Assyrian state plummeted from its zenith (c. 670 BCE) to complete political collapse (c. 615 to 609 BCE). Earlier explanations for the Assyrian collapse focused on the roles of internal politico-economic conflicts, territorial overextension, and military defeat. Here, we present a high-resolution and precisely dated speleothem record of climate change from the Kuna Ba cave in northern Iraq, which suggests that the empire's rise occurred during a two-centuries-long interval of anomalously wet climate in the context of the past 4000 years, while megadroughts during the early-mid seventh century BCE, as severe as recent droughts in the region but lasting for decades, triggered a decline in Assyria's agrarian productivity and thus contributed to its eventual political and economic collapse.

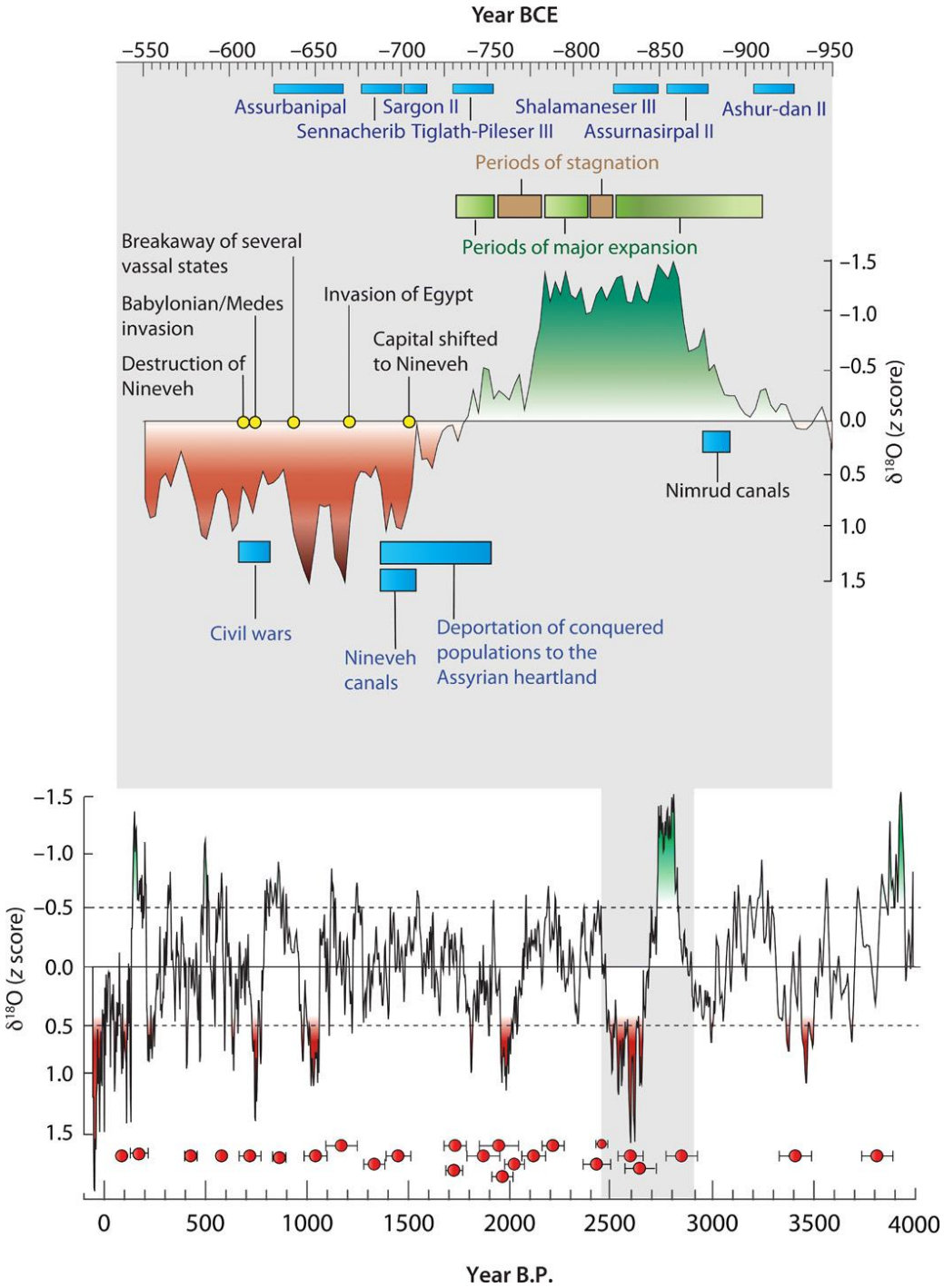

Figure 1. The detrended and normalized $\delta^{18}O$ record (this study) delineates a number of subdecadal to multidecadal periods of inferred drought (z score > 0.5, brown) and pluvial conditions (z score < −0.5, green). The inset shows the $\delta^{18}O$ record between 550 and 950 BCE (shaded, with increasing saturation index representing increasing intensity) and the major historical Assyrian events delineated by horizontal color bars, yellow dots, and supporting text. Approximate reigns of the key Assyrian kings are shown with horizontal bars (cyan). Red circles and error bars mark ^{230}Th dates with 2σ error. The chronology of Neo-Assyrian rulers and imperial events is primarily based on the dating of the Būr-saggilê eponym to the solar eclipse of 15 June 763 BCE (see also the Supplementary Materials for more information) (*27*). The age errors associated with historical events are known with annual and, for many events such as the Fall of Nineveh in 612 BCE, at monthly chronological precision (*27*).